389604-3-T

Barkeshli Kasra

THE UNIVERSITY OF MICHIGAN

COLLEGE OF ENGINEERING

DEPARTMENT OF ELECTRICAL ENGINEERING & COMPUTER SCIENCE

Radiation Laboratory

APPLICATION OF THE CONJUGATE GRADIENT FFT METHOD TO A CLASS OF LARGE RADIATING AND SCATTERING PROBLEMS

Kasra Barkeshli
John L. Volakis
Radiation Laboratory
Department of Electrical Engineering
and Computer Science
The University of Michigan
Ann Arbor, MI 48109

April, 1988

General Dynamics
P.O. Box 748
Fort Worth, TX 76101

Ann Arbor, Michigan


THE UNIVERSITY OF MICHIGAN
LIBRARIES

Abstract

The application of the Conjugate Gradient FFT(CGFFT) method to electrically large radiating and scattering systems is discussed. Results are presented for thin cylindrical dipoles, thin conductive and resistive strips, dielectric cylinders and material plates of various sizes. The extension of the conjugate gradient FFT method to encompass general subdomain expansion functions is also considered. The procedure involves the incorporation of subdomain basis functions associated with the current representation of linear and planar radiating elements. It is shown that significant improvements are achieved in the convergence of the CGFFT method when using sinusoidal basis functions due to a more accurate representation of the current in the spectral domain. In all cases, an increase in the rate of convergence by a factor of two or better was observed. These results are further compared with those obtained by the Moment Method.

Contents

List of Figures

List of Tables

Chapter 1

Introduction and Background

Most integral equations arising in the study of electromagnetic radiation and scattering problems involve a convolution integral. A typical form of such integral equations is

$$\mathbf{E}^{\mathbf{i}}(\mathbf{r}) = \bar{\bar{\eta}}(\mathbf{r}) \cdot \mathbf{J}(\mathbf{r}) + \int_{v'} \bar{\Gamma}(|\mathbf{r} - \mathbf{r}'|) \cdot \mathbf{J}(\mathbf{r}')dv' \quad , \tag{1.1}$$

where $\mathbf{E}^{\mathbf{i}}$ denotes the incident or excitation field vector, $\mathbf{J}$ is the unknown current density vector, $\bar{\Gamma}$ is the associated dyadic Green's function and $\bar{\bar{\eta}}$ is some given tensor specific to the geometry of the problem. Also, $\mathbf{r}$ and $\mathbf{r}'$ are the observation and source position vectors. Alternatively, (1.1) can also be written in an operator form as

$$A[\mathbf{J}] = \mathbf{E}^{\mathbf{i}} \cdot \tag{1.2}$$

Traditionally, the Method of Moments(MOM)[1] has been applied for the solution of (1.2). This involves the discretization of the operator after first introducing an expansion of the current using some basis function. The coefficients of the expansion are then computed via a matrix inversion process. However, the limitations on available computer resources(storage and time) associated with the numerical

formulation of large systems have limited the range of applicability of the MOM. This has prompted some researchers to investigate iterative approaches to the solution of (1.2) including the conjugate gradient method[2],[3] in conjunction with the Fast Fourier Transform(FFT)[4],[5],[6]-[9].

The conjugate gradient method is a nonlinear semi-direct scheme. That is, in the absence of roundoff errors, the exact solution is obtained in a finite number of steps. Also, the solution is improved at a steady rate throughout the iterative process. When combined with the FFT, the conjugate gradient method takes advantage of the convolution theorem reducing the cumbersome computation of the convolution integral to simple algebraic manipulations in the spectral domain. Such a formulation avoids the generation of the square matrix corresponding to operator A and thus implies a storage requirement of $\mathcal{O}(N)$ as compared to $\mathcal{O}(N^2)$ required for an implementation of the MOM. This storage economy has made the formulation suitable for large radiating systems and is a major factor in the capability and potential of the method.

Other iterative methods utilizing the FFT algorithm have also been applied to a number of scattering problems[10]-[12]. However, these techniques usually suffer from two major defficiencies common to most iterative approaches: 1) convergence is not strictly guaranteed and 2) convergence is often slow. The conjugate gradient method virtually eliminates the first problem because it guarantees monotonic convergence throughout the process. As for the second one, the required number of iterations before the conjugate gradient method can yield a reasonable accuracy is often a fraction of the total number of unknowns. This depends primarily on the

distribution of the dominant eigenvalues of the operator projected onto the system matrix. It has been argued convincingly[7] that the conjugate gradient method requires roughly twice as much computation time per solution as the Gaussian elimination-an $\mathcal{O}(N^3)$ operation. However, the CGFFT is considerably faster since it requires only $4N(1 + \log_2 N)$ operations per iteration. This will be discussed later in more detail.

In this report the application of the CGFFT method to several problems of interest in electromagnetics is explored. A brief presentation of the MOM is first given in chapter 2. In chapter 3, the concept of conjugate directions is introduced along with the iterative algorithm utilized in this study. The formulation of the CGFFT method is given next. A considerable portion of this report is devoted to improving the convergence rate of the CGFFT by the incorporation of subdomain basis functions for the expansion of the unknown current distribution. To accomplish this, the current is first expressed as a convolution of the chosen subsectional basis with a finite sequence of delta functions whose amplitudes are the sampled values of the current. By employing this representation in conjunction with the convolution theorem, the CGFFT formulation is extended to general basis functions. A detailed formulation of this procedure is presented in chapter 4. The method is applied to thin cylindrical dipoles, conductive and resistive strips, dielectric cylinders and material plates of various sizes in chapter 5. In all cases, The numerical results are further compared with those obtained by the corresponding direct method. The incorporation of the subsectional basis functions to iterative methods involving the FFT has been previously treated in connection with the

Spectral Iterative Technique(SIT)[13] and has shown to produce improvements in the rate of convergence. However, no quantitative conclusions were drawn because of convergence difficulties associated with the SIT.

In the following chapters a time dependence $e^{j\omega t}$ is understood and suppressed.

Chapter 2

The Method of Moments

In the method of moments the unknown current in (1.2) is expanded in terms of a sequence of known basis functions $\{f_n\}$ as

$$J(x) \simeq \sum_{n=1}^{N} c_n f_n(x), \tag{2.1}$$

where $\{c_n\}$ represents the unknown complex coefficients to be determined. The justification for the validity of the above expansion is discussed in appendix A where the series convergence in the mean square sense has been established for the problems of interest. Substituting (2.1) into (1.2) gives

$$A[\sum_{n=1}^{N} c_n f_n(x)] \simeq E^i(x), \tag{2.2}$$

with a corresponding residual error defined by

$$R = \sum_{n=1}^{N} c_n A[f_n(x)] - E^i(x) \cdot \tag{2.3}$$

The coefficients c_n are computed so that the weighted average of the error on each segment is forced to zero. Thus, by introducing the inner product

$$< f, g >= \int_x f(x)g(x)dx, \tag{2.4}$$

the residual error is orthogonalized with respect to a sequence of weighting functions $\{w_n\}$ such that

$$< w, R >= 0. \tag{2.5}$$

The above represents a system of linear equations

$$\sum_{n=1}^{N} c_n < w_m, A[f_n] >=< w_m, E^i > \quad , \quad m = 1, \cdots, N. \tag{2.6}$$

which can also be put in the matrix form

$$[A_{mn}][c_n] = [E_m^i] \tag{2.7}$$

with

$$A_{mn} =< w_m, A[f_n] > \tag{2.8}$$

and

$$E_m^i =< w_m, E^i > . \tag{2.9}$$

This equation can be solved for the unknown coefficients via matrix inversion to give

$$[c_n] = [A_{mn}]^{-1}[E_m^i]. \tag{2.10}$$

Chapter 3

The Conjugate Gradient Method

The conjugate gradient method is now considered for an iterative solution of (1.2). In general, iterative techniques become more attractive for the solution of operator equations arising in electromagnetic problems as the size of the problem increases. This is mainly because the iterative methods avoid the process of matrix inversion which is subject to numerical instability for ill-conditioned matrices. Also, these schemes often involve only the multiplication of the matrices with vectors and thus do not require an explicit storage of the system matrix.

3.1 Description of the Conjugate Gradient Method

The conjugate gradient method is a nonlinear semi-direct purely-iterative scheme. That is, assuming no truncation and roundoff errors, the exact solution is obtained in a finite number of steps depending on the number of independent eigenvalues of the operator matrix. Moreover, the solution is improved at a steady rate throughout the process and monotonic convergence is guaranteed for a given number of unknowns and as the order of approximation is increased[9]. The method starts out with an initial guess J_0 and a corresponding residual error R_0. In each iteration,

it seeks to minimize the residual vector not only on each local search direction but also over the entire span of search directions. To this end, the solution is expanded in terms of search directions generated by the modified Gram-Schmidt orthogonalization scheme when applied to the sequence of residual vectors as the basis functions[1]. The sequence of search directions, $\{P_n\}$ so constructed are mutually A-orthogonal or conjugate (as opposed to orthogonal)

$$< P_i, A[P_j] >= 0 \quad , \quad i \neq j \quad . \tag{3.1}$$

The significance of this set of directions is as follows: for a quadratic function, successive line minimizations along a conjugate set of directions will achieve the minimum without the need to redo minimization in any direction. Consequently, the minimum is achieved at the end of a finite number of steps. For nonquadratic functions, this guarantees quadratic convergence as the process goes on.

A modified version of the conjugate gradient method suitable for numerical computation is[6],[8]

$$R_0 = A[J_0] - E^i$$

$$P_0 = -b_{-1} A^a[R_0]$$

Main Iteration Loop

$$t_n = \frac{1}{\|A[P_n]\|^2}$$

$$J_{n+1} = J_n + t_n P_n$$

[1]The choice of the n-dimensional coordinate unit vectors as the basis functions would yield Gaussian elimination.

$$R_{n+1} = R_n + t_n A[P_n] \tag{3.2}$$

$$b_n = \frac{1}{\|A^a[R_n]\|^2}$$

$$P_{n+1} = P_n - b_n A^a[R_{n+1}]$$

$$\frac{\|R\|}{\|E^i\|} \stackrel{?}{\leq} \delta$$

Repeat If Necessary

The norm and the adjoint operator are defined in terms of the inner product as

$$\|g\|^2 =< g, g > \tag{3.3}$$

and

$$< A[g], f >=< g, A^a[f] > . \tag{3.4}$$

3.2 Conjugate Gradient FFT Formulation

The convolution involved in (1.2) could be carried out in the frequency domain where it is reduced to algebraic multiplications. Defining the forward and inverse Fourier transform pairs for a one dimensional distribution as

$$\tilde{g}(k_x) = \int_{-\infty}^{\infty} g(x) e^{-jk_x x} dx \tag{3.5}$$

$$\mathcal{F}^{-1}\{\tilde{g}(k_x)\} = g(x) = \int_{-\infty}^{\infty} \tilde{g}(k_x) e^{jk_x x} dk_x \tag{3.6}$$

or

$$\tilde{g}(k_x, k_y) = \int_{-\infty}^{\infty}\int_{-\infty}^{\infty} g(x,y) e^{-j(k_x x + k_y y)} dxdy \tag{3.7}$$

$$\mathcal{F}^{-1}\{\tilde{g}(k_x, k_y)\} = g(x,y) = \int_{-\infty}^{\infty}\int_{-\infty}^{\infty} \tilde{g}(k_x, k_y) e^{j(k_x x + k_y y)} dk_x dk_y \tag{3.8}$$

in the case of a two dimensional one, (1.1) can be alternatively written as

$$\mathbf{E}^{\mathbf{i}} = \bar{\bar{\eta}} \cdot \mathbf{J} + \mathcal{F}^{-1}\{\tilde{\bar{\bar{\Gamma}}} \cdot \tilde{\mathbf{J}}\} \quad . \tag{3.9}$$

Clearly, (3.9) avoids the generation of the square matrix corresponding to operator A and thus implies a storage requirement of $\mathcal{O}(N)$ as compared to $\mathcal{O}(N^2)$ required for an implementation of the MOM. This represents a major advantage of the formulation for the solution of large radiating systems where the size of the associated matrix becomes prohibitively large.

Because of the implied Fourier transforms, a solution of (3.9) via the conjugate gradient method is referred to as the CGFFT method.

Chapter 4

Extension of the CGFFT to General Basis Functions

In the application of the MOM, the use of an appropriate basis function for representing the unknown current distribution plays an important role in the accuracy and efficiency of the solution. Therefore, of interest is the incorporation of a similar representation of the current in conjunction with the CGFFT procedure. Below, an interpretation of the Discrete Fourier Transform(DFT) consistent with the usual implementation of the FFT for continuous functions is first given. Subsequently, a representation of the current in terms of general basis functions suitable for implementation in the CGFFT formulation is considered.

To perform a numerical computation of the Fourier transform of a continuous function $J(x)$, a discrete function is first formed by sampling the original one at equally spaced points. The resulting function can then be written as a δ-train of the form

$$J_\delta = \sum_{n=1}^{N} J_n \delta(x - x_n) \quad , \tag{4.1}$$

where $\delta(x)$ is the usual Dirac delta function and $J_n = J(x_n)$. To establish a rela-

tionship between the Fourier transform of a continuous function and its associated discrete transform, the function is first expanded in a sequence of subsectional basis functions $\{f_n\}$ as

$$\begin{aligned} J(x) &= \sum_{n=1}^{N} J_n f_n(x) \\ &= \sum_{n=1}^{N} J_n f(x - x_n) \cdot \end{aligned} \tag{4.2}$$

Customary forms of the basis function f include the piecewise constant(PWC) and the overlapping piecewise sinusoidal(PWS) expansion functions given by

$$P(x) = \begin{cases} 1 & , |x| \leq \Delta/2 \\ 0 & , else \end{cases} \tag{4.3}$$

$$S(x) = \begin{cases} \frac{\sin[k_0(\Delta - |x|)]}{\sin(k_0 \Delta)} & , |x| \leq \Delta \\ 0 & , else \end{cases} , \tag{4.4}$$

respectively. Combining (4.1) and (4.2), $J(x)$ can be written as a convolution in the form

$$J(x) = f(x) * \sum_{n=1}^{N} J_n \delta(x - x_n) \quad \cdot \tag{4.5}$$

The Fourier transform of J is thus given by

$$\tilde{J}(k_x) = \tilde{f}(k_x) \widehat{J_\delta} \quad \cdot \tag{4.6}$$

In the above, $\tilde{f}$ and $\widehat{J_\delta}$ are the Fourier transforms of the chosen basis function f and the discrete function J_δ, respectively. For the above two choices in (4.3) and (4.4),

$$\tilde{P}(k_x) = (\Delta) \frac{\sin(k_x \Delta/2)}{k_x \Delta/2} \quad , \tag{4.7}$$

$$\tilde{S}(k_x) = \frac{2k_0[\cos(k_x \Delta) - \cos(k_0 \Delta)]}{\sin(k_0 \Delta)(k_0^2 - k_x^2)} \quad \cdot \tag{4.8}$$

In evaluating $\widehat{J_\delta}$, it is assumed that the N samples $\{J_n\}$ of the original function are one period of a periodic waveform whose Fourier transform is given by

$$\widehat{J_\delta}_k = \sum_{m=1}^{N} J_m e^{-2\pi jmk/N} \quad k = 1, \cdots, N \tag{4.9}$$

and is commonly known as the discrete Fourier transform.

As a corolary, it is important to note that for a sufficiently small sampling interval ($\lim_{\Delta \to 0} \tilde{f}(k_x) = \Delta$) the relation

$$\tilde{J} \simeq \Delta \widehat{J_\delta} \tag{4.10}$$

holds when the above expansion functions are employed. Equation (4.10) establishes the connection between the analytical and discrete Fourier transforms of the current when the sampling interval is sufficiently small. Since the same result can also be derived via direct application of the rectangular rule of integration in the computation of the Fourier integral, (4.10) has been exclusively associated with the piecewise constant basis functions in the application of the FFT algorithm despite the fact that it holds true for all subsectional expansions. As will be shown later, the convergence of the CGFFT method is improved considerably if the more accurate expression (4.6) is used in the formulation instead of (4.10).

In the case of a two dimensional current representation, an appropriate expansion is

$$J(x,y) = f(x,y) * \sum_{n=1}^{N} \sum_{m=1}^{M} J_{nm} \delta(x - x_n, y - y_m) \tag{4.11}$$

where $f(x,y)$ denotes the surface basis function and $J_{nm} = J(x_n, y_m)$. The corresponding Fourier transform is

$$\tilde{J}(k_x, k_y) = \tilde{f}(k_x, k_y) \widehat{J_\delta} \tag{4.12}$$

and consistent with the previous notation, the tilde and hat denote the two dimensional Fourier and discrete Fourier transforms, respectively. The two dimensional piecewise constant and sinusoidal basis functions are given by

$$P(x,y) = P(x)P(y) = \begin{cases} 1 & ,on\ \ \Delta s \\ 0 & ,else \end{cases} \tag{4.13}$$

$$S(x,y) = S(x)S(y) = \begin{cases} \frac{\sin[k_0(\Delta x - |x|)]}{\sin k_0 \Delta x} \cdot \frac{\sin[k_0(\Delta y - |y|)]}{\sin k_0 \Delta y} & ,on\ \ \Delta s \\ 0 & ,else \end{cases} \tag{4.14}$$

where Δs denotes the area of the surface element. Their corresponding spectra are

$$\tilde{P}(k_x,k_y) = \tilde{P}(k_x)\tilde{P}(k_y) = \Delta s \frac{\sin(k_x\Delta x/2)}{k_x\Delta x/2}\frac{\sin(k_y\Delta y/2)}{k_y\Delta y/2} \tag{4.15}$$

$$\tilde{S}(k_x,k_y) = \tilde{S}(k_x)\tilde{S}(k_y) = \frac{2k_0[\cos(k_x\Delta x) - \cos(k_0\Delta x)]}{\sin(k_0\Delta x)(k_0^2 - k_x^2)} \times \frac{2k_0[\cos(k_y\Delta y) - \cos(k_0\Delta y)]}{\sin(k_0\Delta y)(k_0^2 - k_y^2)} \quad , \tag{4.16}$$

and as $\Delta s \rightarrow 0$, (4.12) reduces to

$$\tilde{J} \simeq \Delta s \widehat{J_\delta} \cdot \tag{4.17}$$

Using (4.6) or (4.12), (3.9) can now be written as

$$\mathbf{E^i} = \bar{\bar{\eta}} \cdot \mathbf{J} + \mathcal{F}^{-1}\{\tilde{\bar{\bar{\Gamma}}} \cdot \tilde{f}\widehat{\mathbf{J}_\delta}\} \cdot \tag{4.18}$$

Clearly, the transform $\tilde{f}$ of the basis function needs to be computed only once and thus the computations per iteration implied by (3.9) and (4.18) are essentially the same. It should of course be noted that (4.18) is valid only on the body of the scatterer, a condition that is imposed on the numerical solution along with the sampling requirements and linearity of the corresponding discrete convolution[5].

These numerical considerations are briefly discussed in appendix B. Next, the application and convergence behavior of the CGFFT formulation of (4.18) for various problems involving one and two dimensional current distributions is examined.

Chapter 5

Applications and Results

5.1 Radiation by a Thin Wire Antenna

As a first example, a center-fed cylindrical wire dipole of length l and radius a oriented along the z axis is considered. The scattered field due to the current excited in the dipole is

$$\mathbf{E}^s = (k_0^2 + \nabla\nabla\cdot)\mathbf{\Pi}(\mathbf{r}) \tag{5.1}$$

subject to the boundary condition on the total tangential electric field that

$$E_t^T = E_t^s + E_t^i = 0 \cdot \tag{5.2}$$

In (5.2), $\mathbf{\Pi}$ is the electric Hertz vector potential given by

$$\mathbf{\Pi}(\mathbf{r}) = -\frac{jZ_0}{k_0}\int_{v'} \mathbf{J}(\mathbf{r}')G(\mathbf{r};\mathbf{r}')dv', \tag{5.3}$$

where $Z_0 = 120\pi$ and k_0 are the free space intrinsic impedance and wave number, respectively.

Under the thin wire approximations ($ka << 1$ and $a < l$), the current flow is assumed to be directed only along the z axis and the azimuthal variation of the current is neglected. Thus, the well known Pocklington's integral equation is

obtained

$$E^i(z) = \frac{jZ_0}{k_0}(k_0^2 + \frac{\partial^2}{\partial z^2}) \int_{-l/2}^{l/2} I(z')G(z;z')dz', \tag{5.4}$$

where I is the total wire current and G is the Green's function

$$G(z;z') = \frac{1}{2\pi} \int_0^{2\pi} \frac{e^{-jkR}}{4\pi R} d\phi \tag{5.5}$$

with

$$R = \sqrt{(z-z')^2 + 4a^2 \sin^2 \frac{\phi}{2}} \quad . \tag{5.6}$$

For the Pocklington's equation, the adjoint operator takes the form[9]

$$A^a[I] = -\frac{jZ_0}{k_0}(k_0^2 + \frac{\partial^2}{\partial z^2}) \int_{-l}^{l} G^*(z;z')I(z')dz' \tag{5.7}$$

where $*$ denotes complex conjugate.

Employing now a subsectional basis expansion for the current representation, (5.4) becomes

$$E_z^i(z) = \frac{jZ_0}{k_0} \mathcal{F}^{-1}\{\tilde{\mathcal{K}}(k_z)\hat{I}_\delta\} \tag{5.8}$$

where

$$\tilde{\mathcal{K}}(k_z) = (k_0^2 - k_z^2)\tilde{G}(k_z)\tilde{f}(k_z) \tag{5.9}$$

and

$$\tilde{G}(k_z) = \frac{1}{2\pi} I_0(a\sqrt{k_z^2 - k_0^2}) K_0(a\sqrt{k_z^2 - k_0^2}) \quad , \tag{5.10}$$

in which I_0 and K_0 are the zeroth order modified Bessel functions of the first and second kind, respectively. The corresponding adjoint operator (5.7) is similarly expressed as

$$A^a[I] = -\frac{jZ_0}{k_0} \mathcal{F}^{-1}\{\tilde{\mathcal{K}}\tilde{G}^*\hat{I}_\delta\} \cdot \tag{5.11}$$

Figures 5.1 to 5.4 show the antenna current distributions for a 1λ thin wire dipole of radius $a = .005\lambda$ evaluated by the CGFFT method and the MOM. The tolerance on the normalized residual error for the CGFFT solution was set at 0.3%. Two excitation models were used in the analyses: the voltage gap model and the magnetic frill model. These are discussed in appendix C. For a given excitation, the two methods exhibit similar sampling requirements in order to converge to the correct solution. The same observation was further noted when the input impedance was computed via the two methods as a function of the sampling density(Fig. 5.5). As expected, the results from the two analyses converge to the same value for a sufficiently small sampling interval.

Figure 5.6 shows a comparison between the antenna current distribution for a 9λ thin wire dipole($a = .005\lambda$) using the CGFFT method with different basis functions and that obtained by the MOM. The convergence patterns for the 9λ dipole is depicted in figure 5.7. Clearly, the use of piecewise sinusoidal basis functions is seen to reduce the number of iterations by approximately a factor of two. Also, the improvement in the iteration ratio(the required number of iterations divided by the number of unknowns) for the 1λ dipole considered before is shown in figure 5.8.

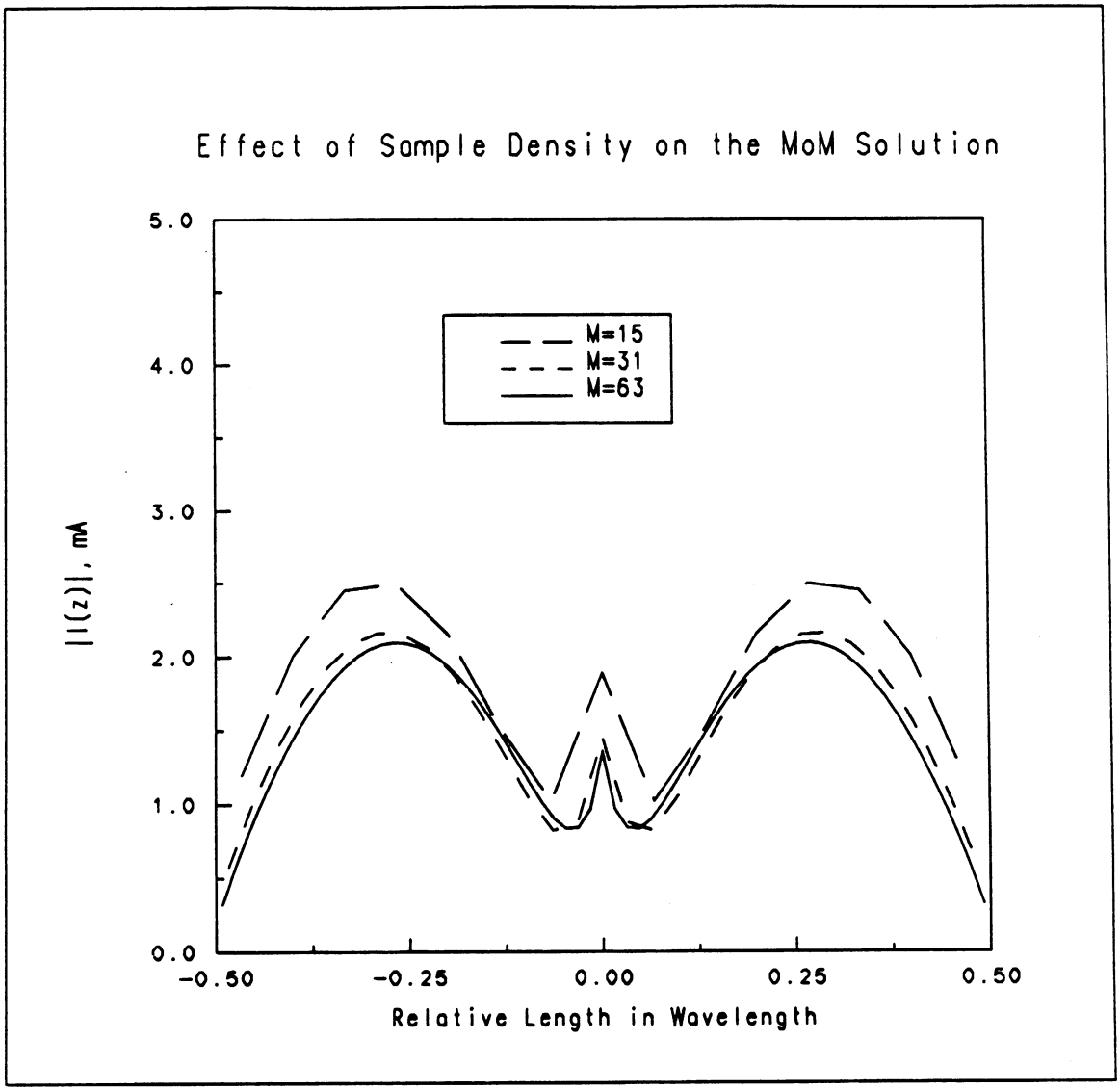

Figure 5.1: Numerical convergence of the linear current distribution for a 1λ dipole with increasing sampling density evaluated by the MOM. Top to bottom: M=15,31,63,127; Voltage gap model.

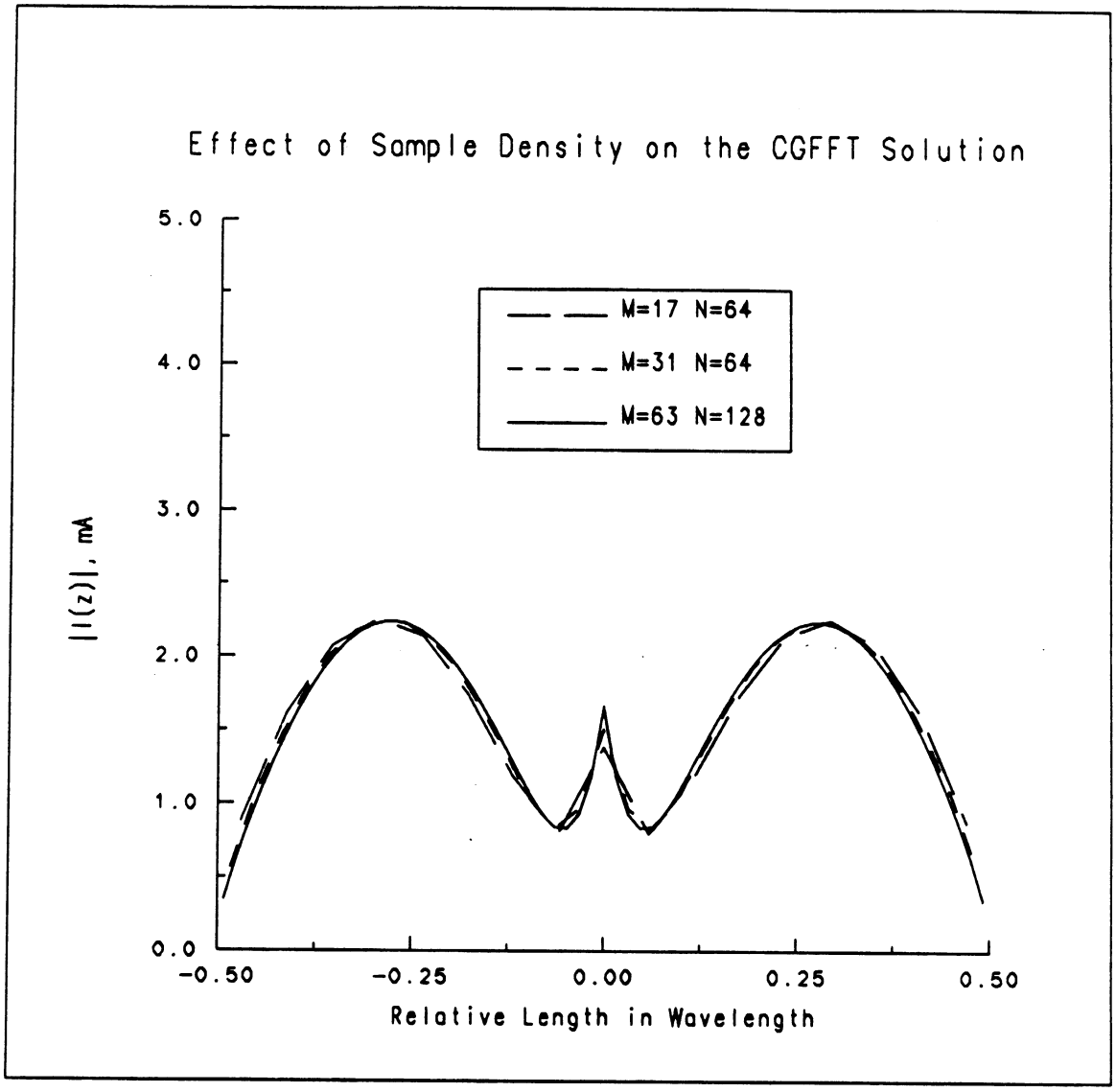

Figure 5.2: **Numerical convergence of the linear current distribution for a 1λ dipole with increasing sampling density evaluated by the CGFFT. Top to bottom: M=15,31,63,127; FFT pad order=2,2,2,1; Voltage gap model.**

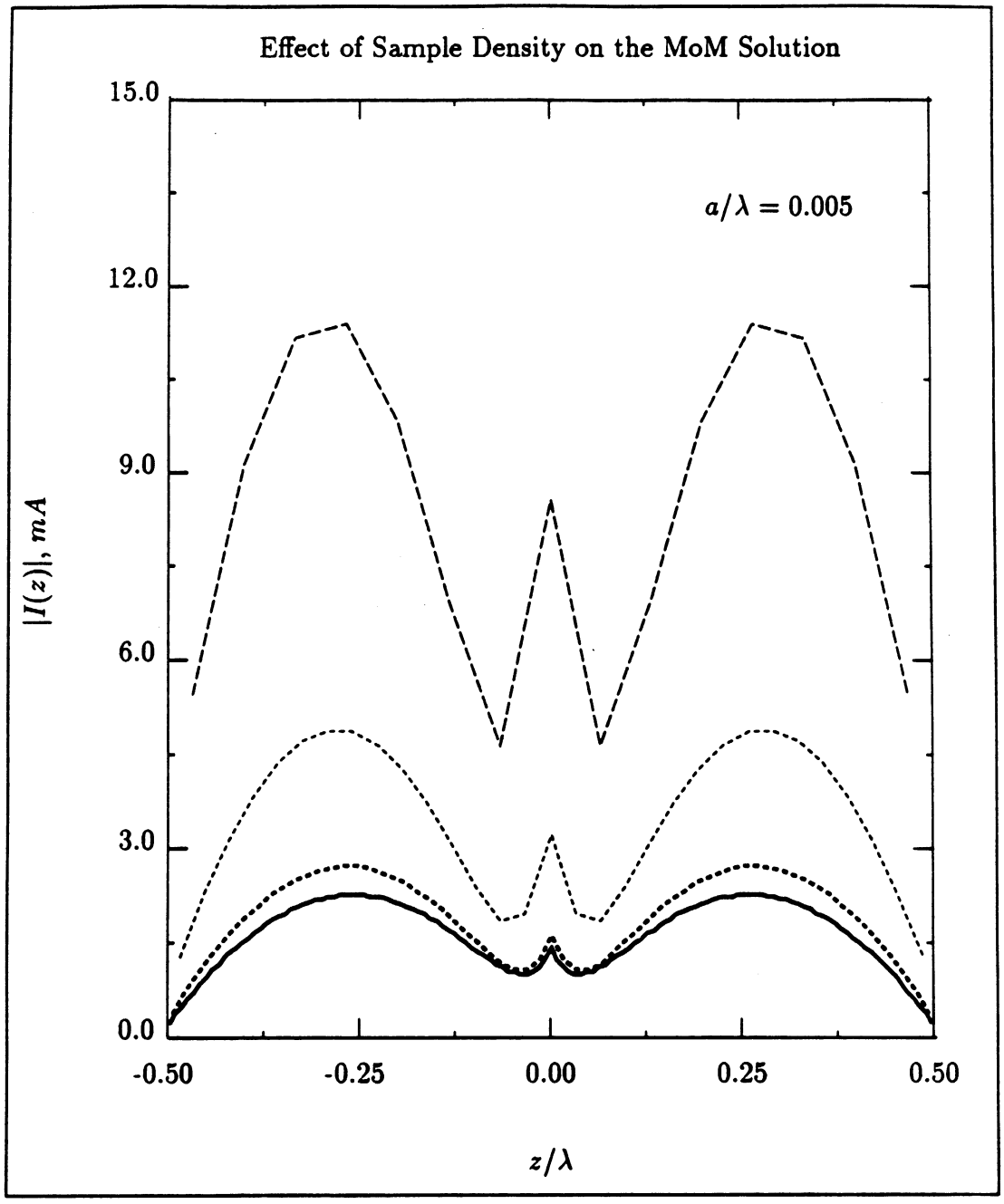

Figure 5.3: Numerical convergence of the linear current distribution for a 1λ dipole with increasing sampling density evaluated by the MOM. Top to bottom: M=15,31,63,127; Magnetic frill model.

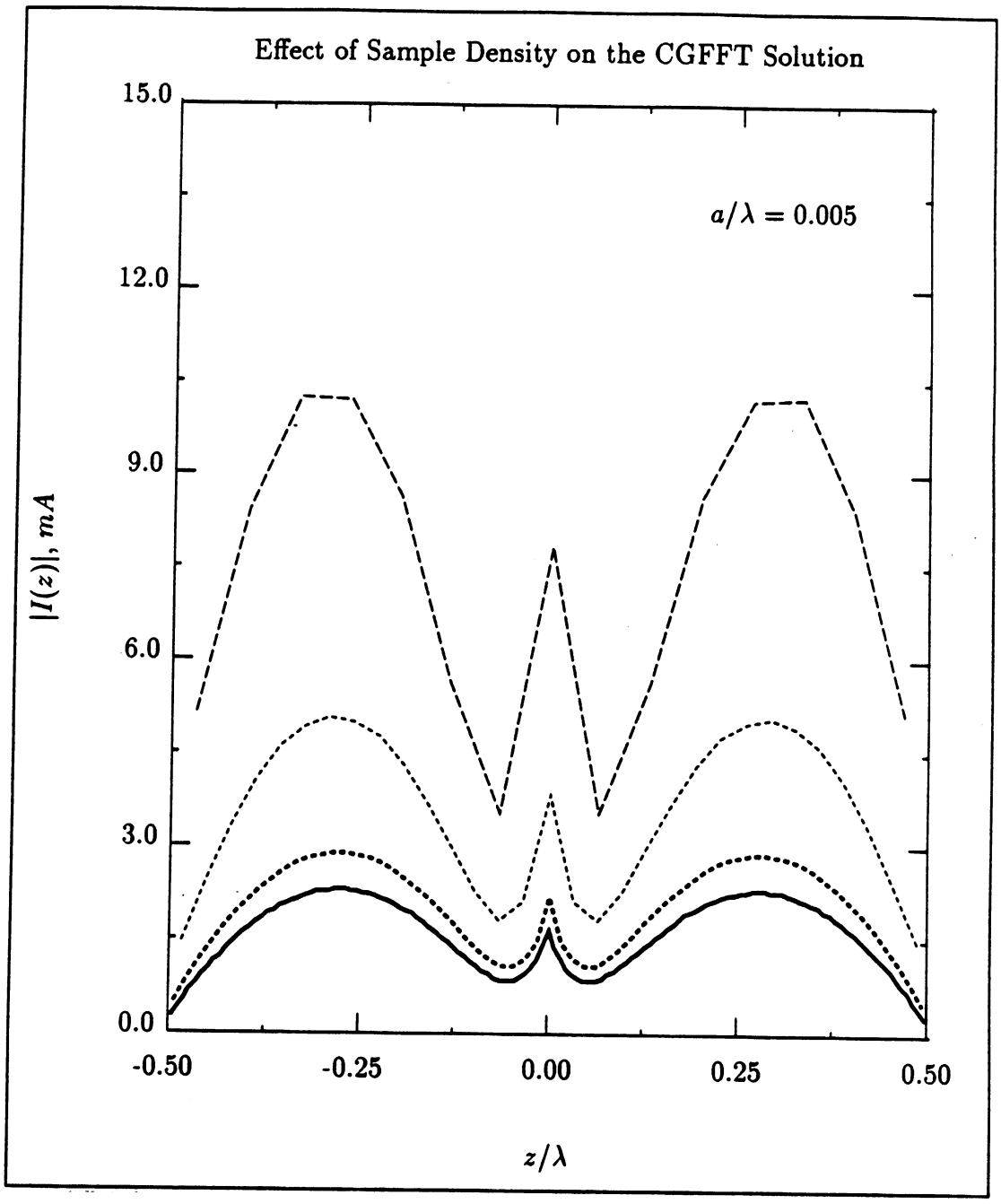

Figure 5.4: Numerical convergence of the linear current distribution for a 1λ dipole with increasing sampling density evaluated by the CGFFT. Top to bottom: M=15,31,63,127; FFT pad order=2,2,2,1; Magnetic frill model.

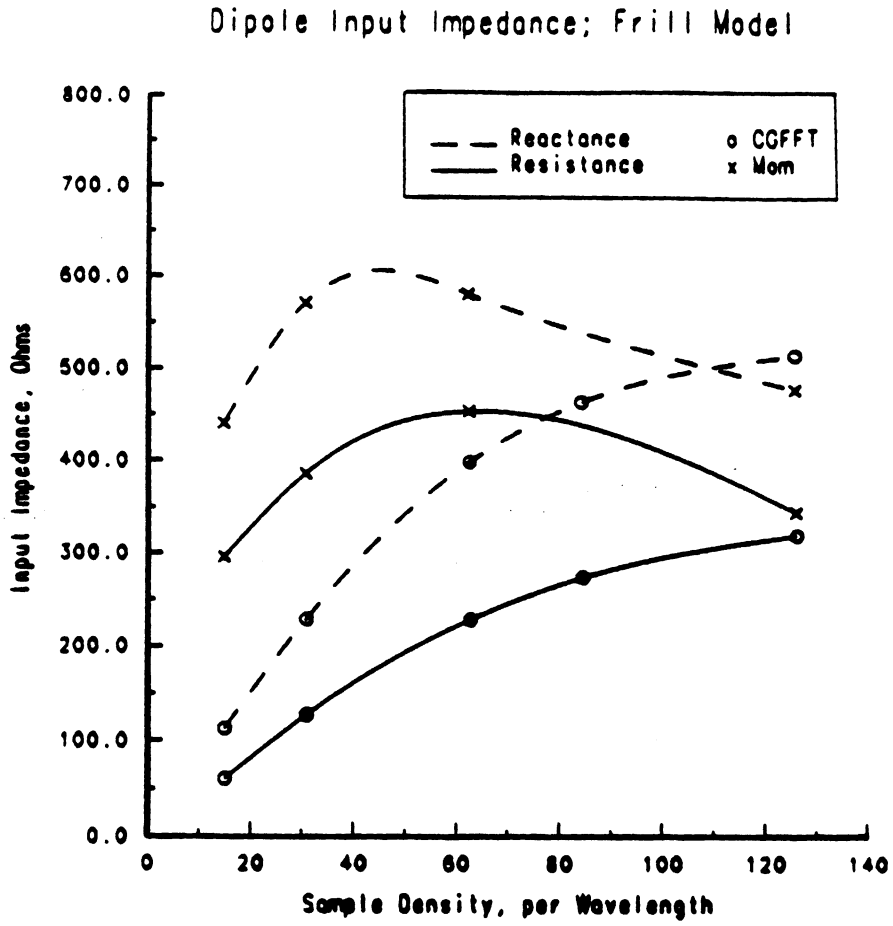

Figure 5.5: Real and imaginary parts of the input impedance for the 1λ dipole($a/\lambda = .005$) as a function of sampling frequency.

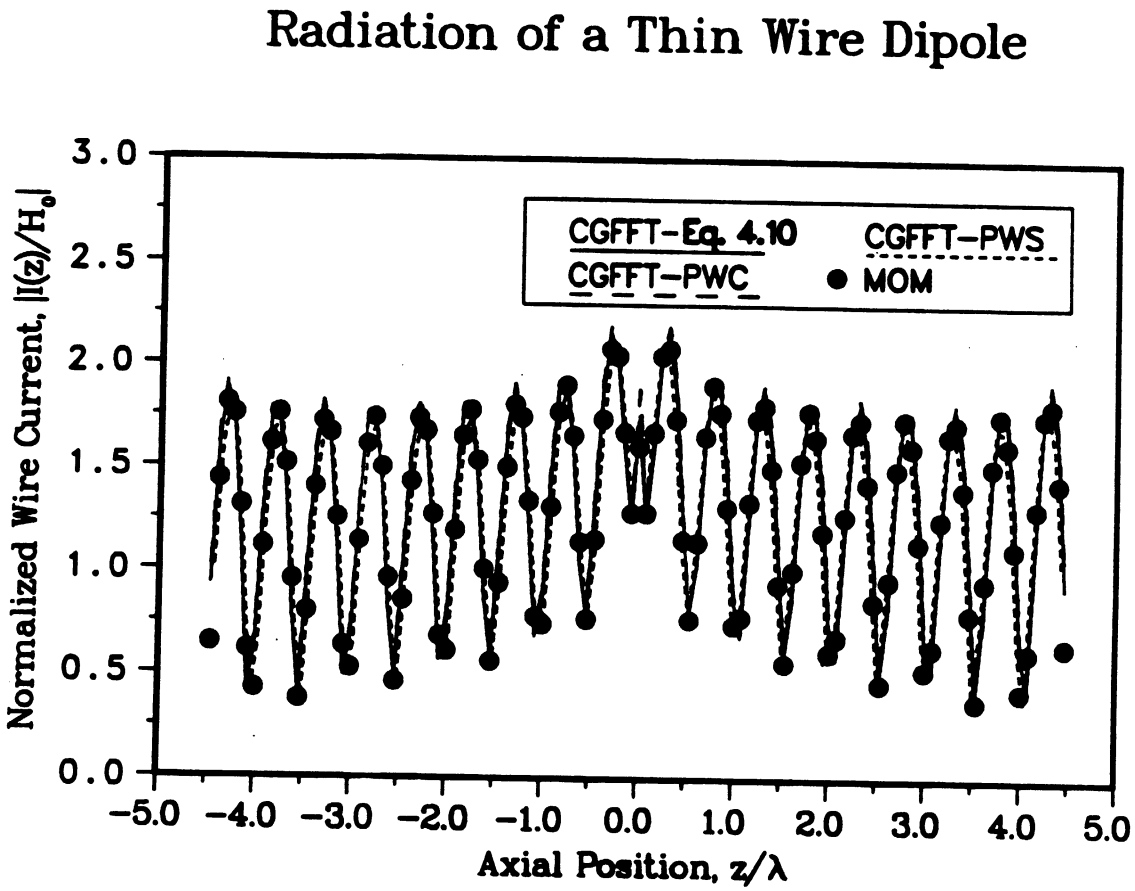

Figure 5.6: Current magnitude for a 9λ dipole($a = .005\lambda$) computed by the MOM and the CGFFT using different basis functions and a voltage gap model for the source(13 unknowns/λ).

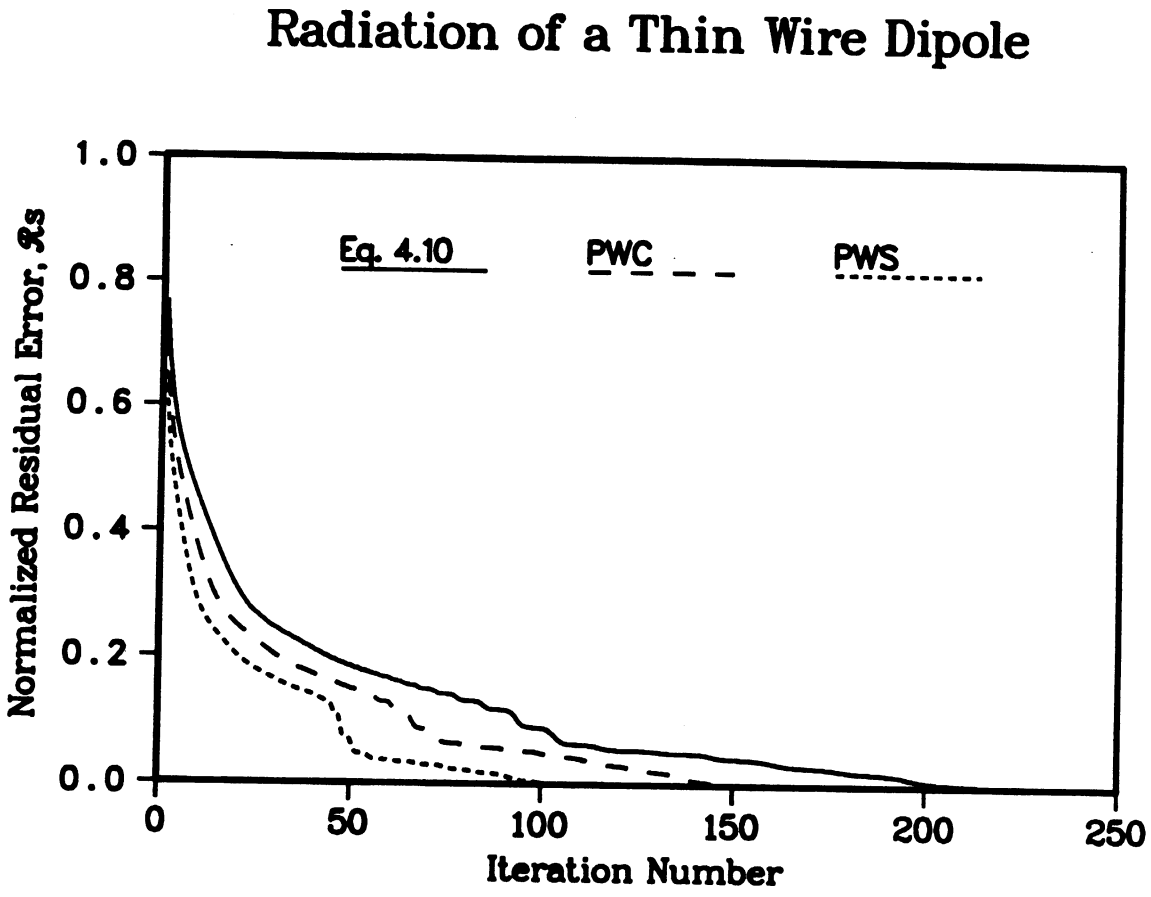

Figure 5.7: Convergence patterns for the 9λ wire dipole(13 unknowns/λ).

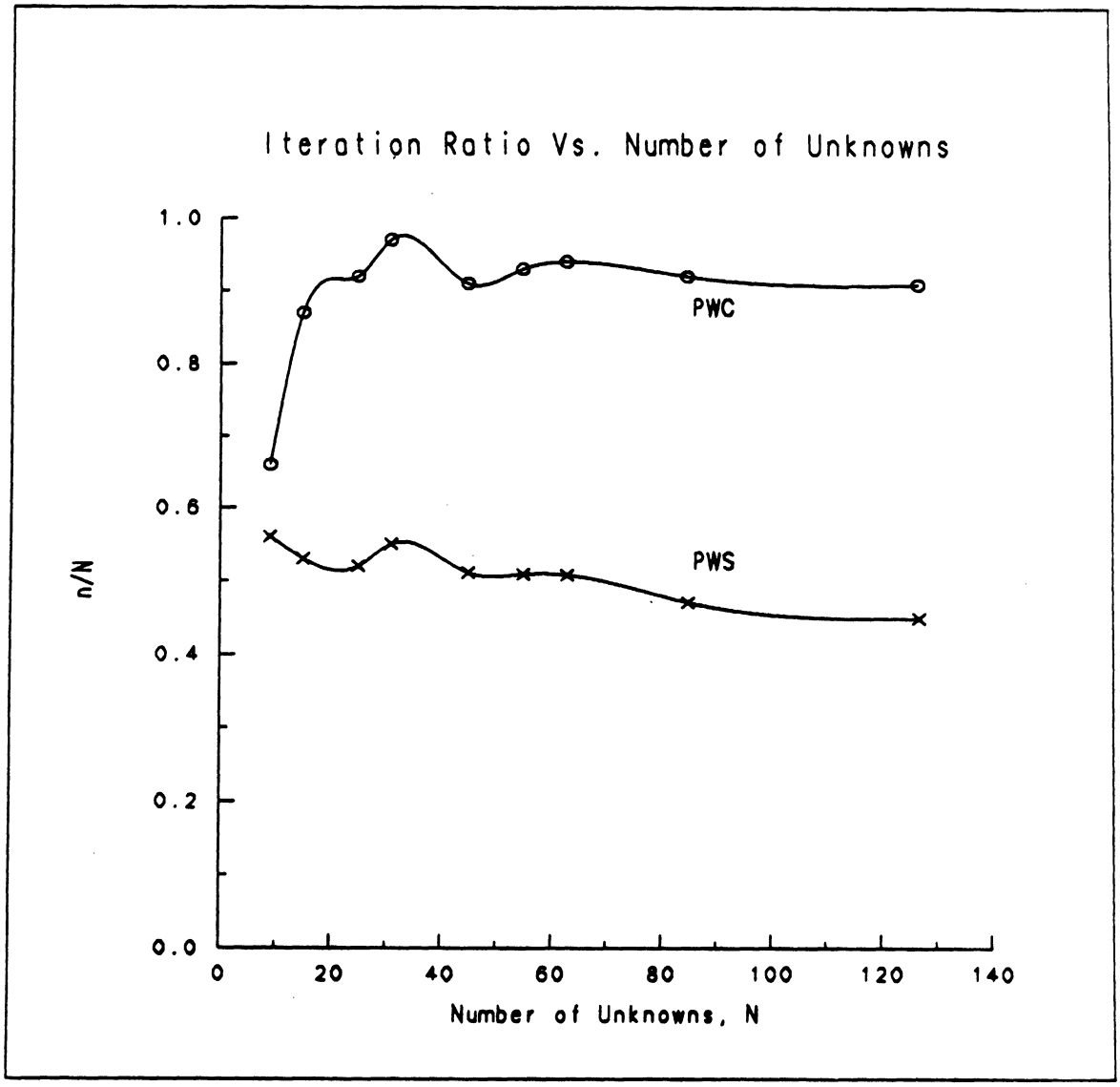

Figure 5.8: The improvement in the iteration ratio for the 1λ wire dipole($a = .005\lambda$) as a function of the number of unknowns.

5.2 Scattering by a Thin Strip

The integral equation for a thin perfectly conducting strip of width w lying on the xz plane(Fig. 5.9) is obtained by imposing the boundary condition demanding that the total tangential electric field vanishes on the strip(as in (5.1) and (5.2).

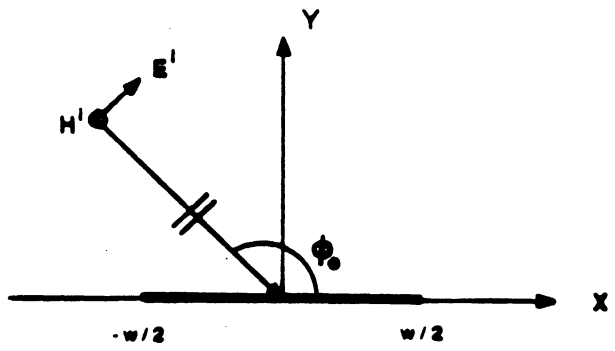

Figure 5.9: Geometry of a perfectly conducting strip illuminated by a plane wave.

For an E-polarized plane wave incidence,

$$\mathbf{E}^{\mathrm{i}} = \hat{z} E_0 e^{jk_0(x\cos(\phi_0) + y\sin(\phi_0))} \tag{5.12}$$

and

$$H_0 e^{jk_0 x\cos(\phi_0)} = \frac{k_0}{4}\int_{-w/2}^{w/2} J_z(x') H_0^{(2)}(k_0|x-x'|)dx' \tag{5.13}$$

where ϕ_0 and ϕ denote the angles of incidence and observation, $H_0^{(2)}$ is the zeroth order Hankel function of the second kind and $\mathbf{J}(x)$ is the unknown current density on the surface of the strip. Similarly, for the H-polarization,

$$\mathbf{H}^{\mathrm{i}} = \hat{z} H_0 e^{jk_0(x\cos(\phi_0) + y\sin(\phi_0))} \tag{5.14}$$

and

$$H_0 e^{jk_0 x\cos(\phi_0)} = \frac{1}{4k_0}(k_0^2 + \frac{\partial^2}{\partial x^2})\int_{-w/2}^{w/2} J_x(x')H_0^{(2)}(k_0|x-x'|)dx' \cdot \qquad (5.15)$$

Applying the same procedure discussed for the dipole problem, the integral equations take the form

$$H_0 e^{jk_0 x\cos(\phi_0)} = \frac{1}{4k_0}\mathcal{F}^{-1}\{\widetilde{\mathcal{W}}(k_x)\widehat{J_\delta}\} \qquad (5.16)$$

where

$$\widetilde{\mathcal{W}}(k_x) = \begin{cases} k_0^2\widetilde{H}_0^{(2)}(k_x)\tilde{f}(k_x) & , E-pol. \\ (k_0^2 - k_x^2)\widetilde{H}_0^{(2)}(k_x)\tilde{f}(k_x) & , H-pol. \end{cases} \qquad (5.17)$$

and

$$\widetilde{H}_0^{(2)}(k_x) = \frac{2}{\sqrt{k_0^2 - k_x^2}} \cdot \qquad (5.18)$$

The two dimensional radar cross section(echo width) is defined as

$$\sigma(\phi) = \lim_{\rho\to\infty} 2\pi\rho\frac{|E^s(\phi)|^2}{|E^i(\phi)|^2} \cdot \qquad (5.19)$$

Using the asymptotic large argument approximation to the Hankel function($\lim_{k\rho\to\infty}$)

$$H_0^{(2)}(k\rho) \sim \sqrt{\frac{2}{\pi k}}e^{j\pi/4}\frac{e^{-jk\rho}}{\sqrt{\rho}} \quad , \qquad (5.20)$$

equation (5.19) takes the forms

$$\sigma_E(\phi) = \frac{k_0}{4H_0^{(2)}}|\int_{-w/2}^{w/2} J_z(x')e^{jkx'\cos\phi}dx'|^2 \qquad (5.21)$$

and

$$\sigma_H(\phi) = \frac{k_0}{4H_0^{(2)}}|\sin\phi\int_{-w/2}^{w/2} J_x(x')e^{jkx'\cos\phi}dx'|^2 \qquad (5.22)$$

for E and H polarizations, respectively.

Figure 5.10 shows a comparison of the computed surface current density of a 4λ conducting strip for the H-polarization at normal incidence as obtained by the CGFFT and the MOM. The bistatic echowidth for this case is shown in figure 5.11. The backscatter echowidth for the same strip as computed by the two methods is also given in figure 5.12 for verification purposes. As before, the convergence rate is increased by a factor of two when employing the piecewise sinusoidal basis function as shown in figure 5.13.

This formulation can be easily extended to tapered resistive strips. Allowing dielectric variations only along the width of the strip, the resistivity for a thin strip of thickness τ and relative permittivity ϵ_r is defined by

$$R(x) = \frac{1}{j\omega\epsilon_0(\epsilon_r(x) - 1)\tau}. \tag{5.23}$$

The total tangential electric field is now written as

$$E_t^T = R(x)J(x) \tag{5.24}$$

and the integral equations for the E and H polarizations are expressed as

$$H_0 e^{jk_0 x\cos(\phi_0)} = \eta(x)J_z(x) + \frac{k_0}{4}\int_{-w/2}^{w/2} J_z(x')H_0^{(2)}(k_0|x - x'|)dx' \tag{5.25}$$

and

$$H_0 e^{jk_0 x\cos(\phi_0)} = \eta(x)J_x(x) + \frac{1}{4k_0}(k_0^2 + \frac{\partial^2}{\partial x^2})\int_{-w/2}^{w/2} J_x(x')H_0^{(2)}(k_0|x - x'|)dx', \tag{5.26}$$

respectively. In the above, $\eta(x)$ denotes the normalized strip resistivity

$$\eta(x) = \frac{R(x)}{Z_0}. \tag{5.27}$$

Application of the extended CGFFT formulation to these integral equations follows in the same manner as before except for the presence of the terms involving the surface current densities outside the integrals.

Figures 5.14 and 5.15 show the results for a strip which is tapered parabolically, that is

$$\eta(x) = \eta_c + \eta_e|\frac{x}{w/2}|^2 \cdot \tag{5.28}$$

in (5.28), η_c and η_e denote the resistivity at the center and the edges of the strip, respectively. The results obtained by the moment method are also shown in those figures. In practice, tapering of the strip resistivity is used to lower the sidelobe levels as can be seen from figures 5.16 and 5.17 where the backscattering echowidths of the tapered strip is compared with those of the perfectly conducting one for both polarizations.

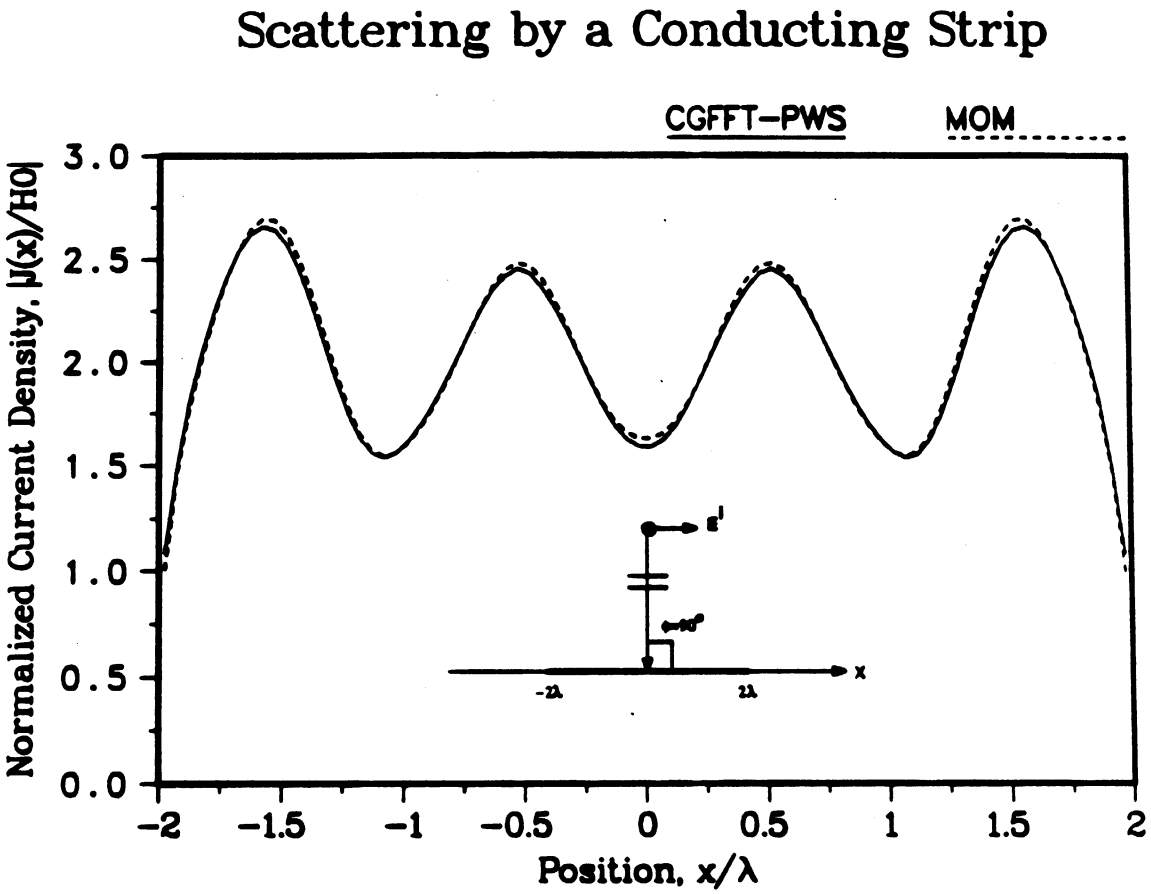

Figure 5.10: Surface current density magnitude for a 4λ strip illuminated with an H-polarized plane wave at normal incidence computed by the MOM and the CGFFT using piecewise sinusoidal basis functions(20 unknowns/λ).

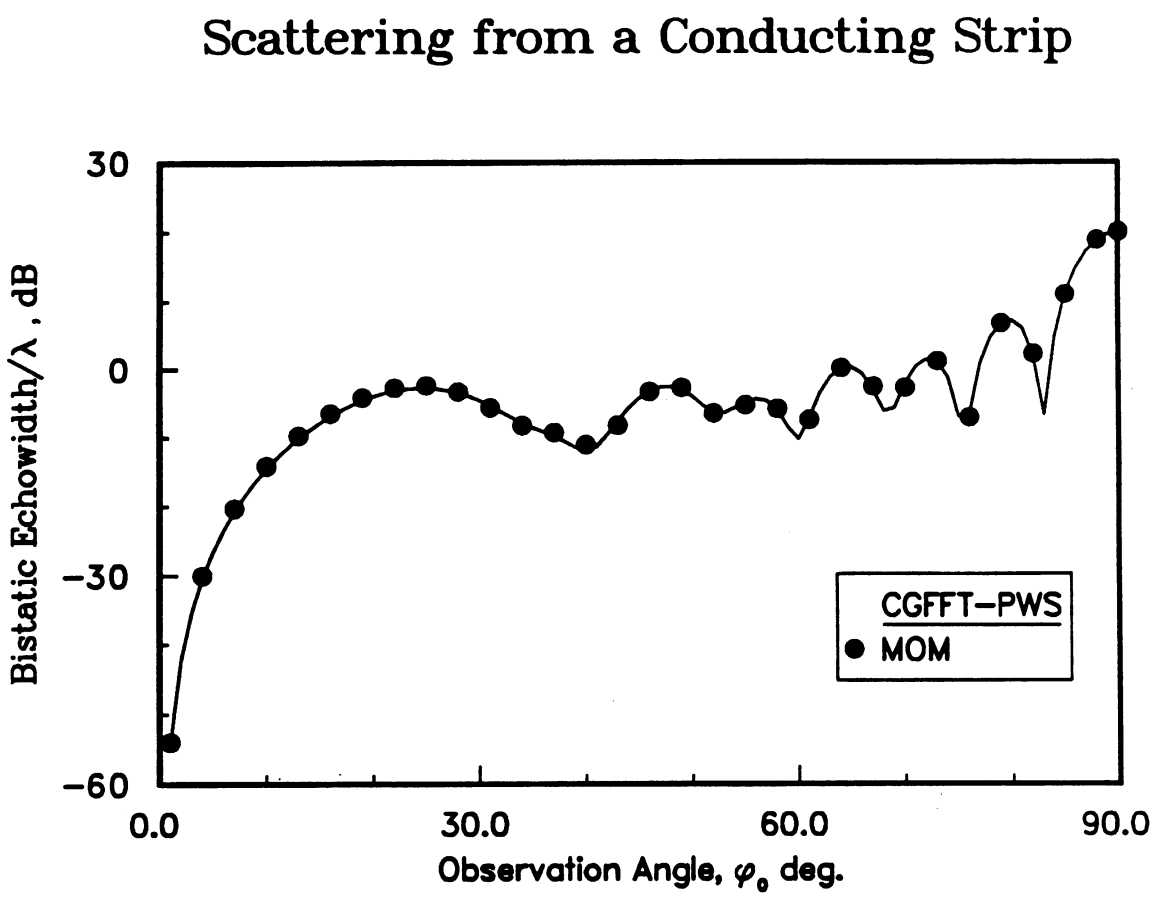

Figure 5.11: Bistatic echowidth of the 4λ strip illuminated with an H-polarized plane wave at normal incidence.

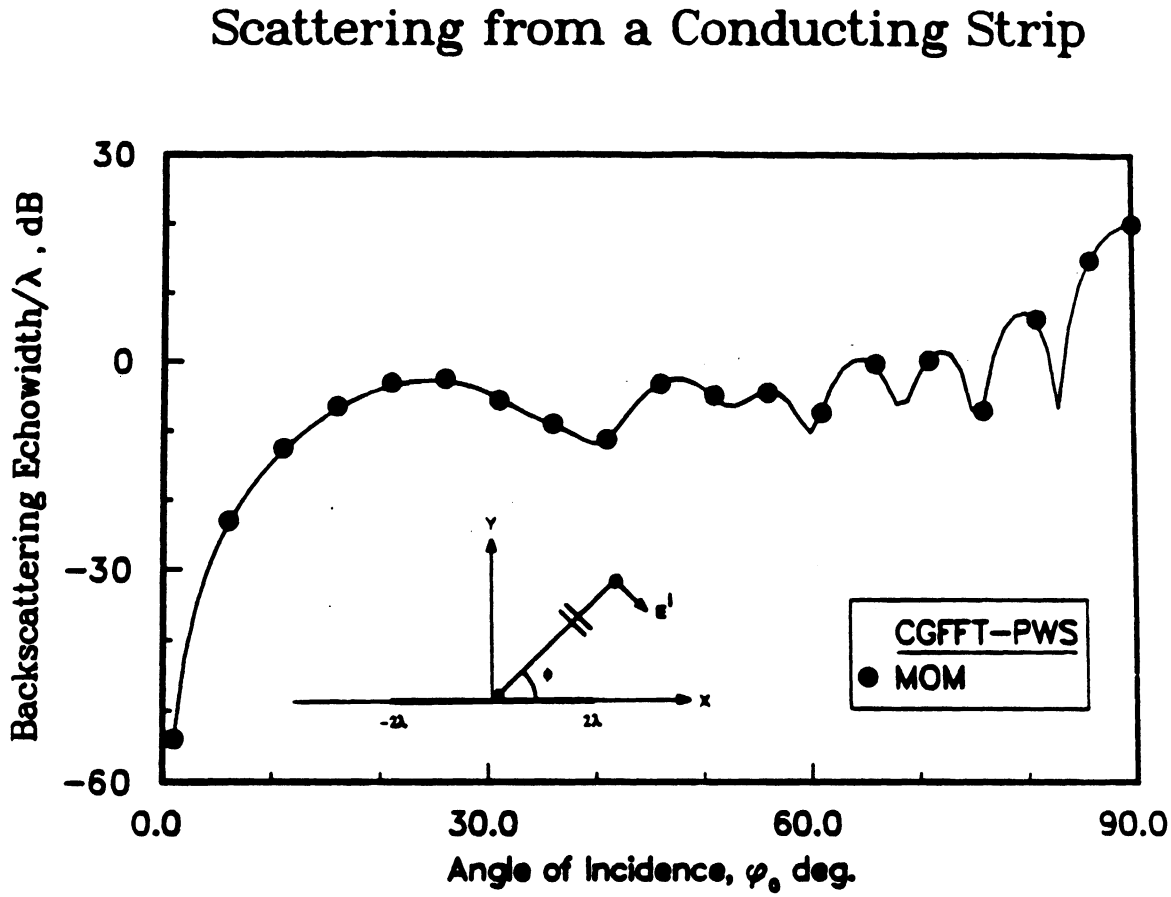

Figure 5.12: Backscatter echowidth of the 4λ strip illuminated with an H-polarized plane wave.

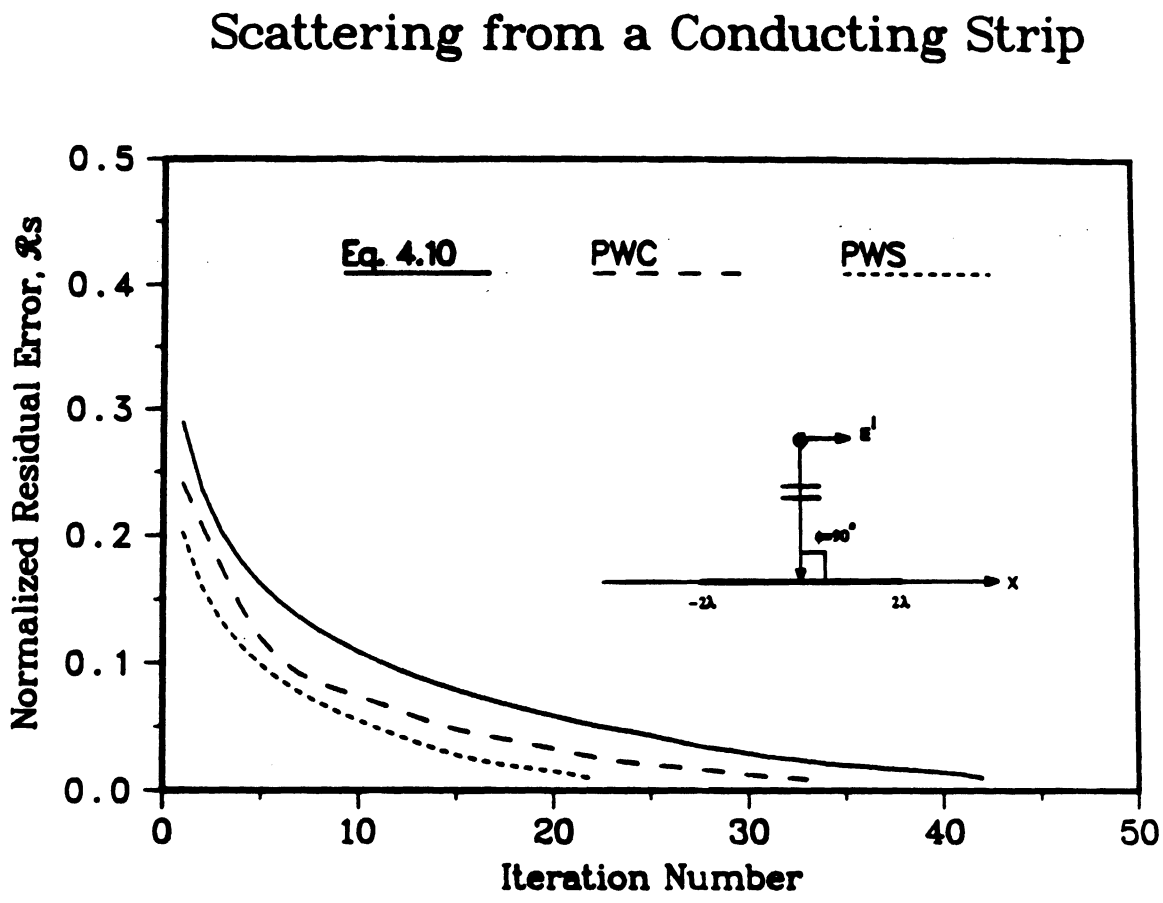

Figure 5.13: Convergence patterns for a 4λ conducting strip illuminated by an H-polarized plane wave at normal incidence using 20 unknowns/λ.

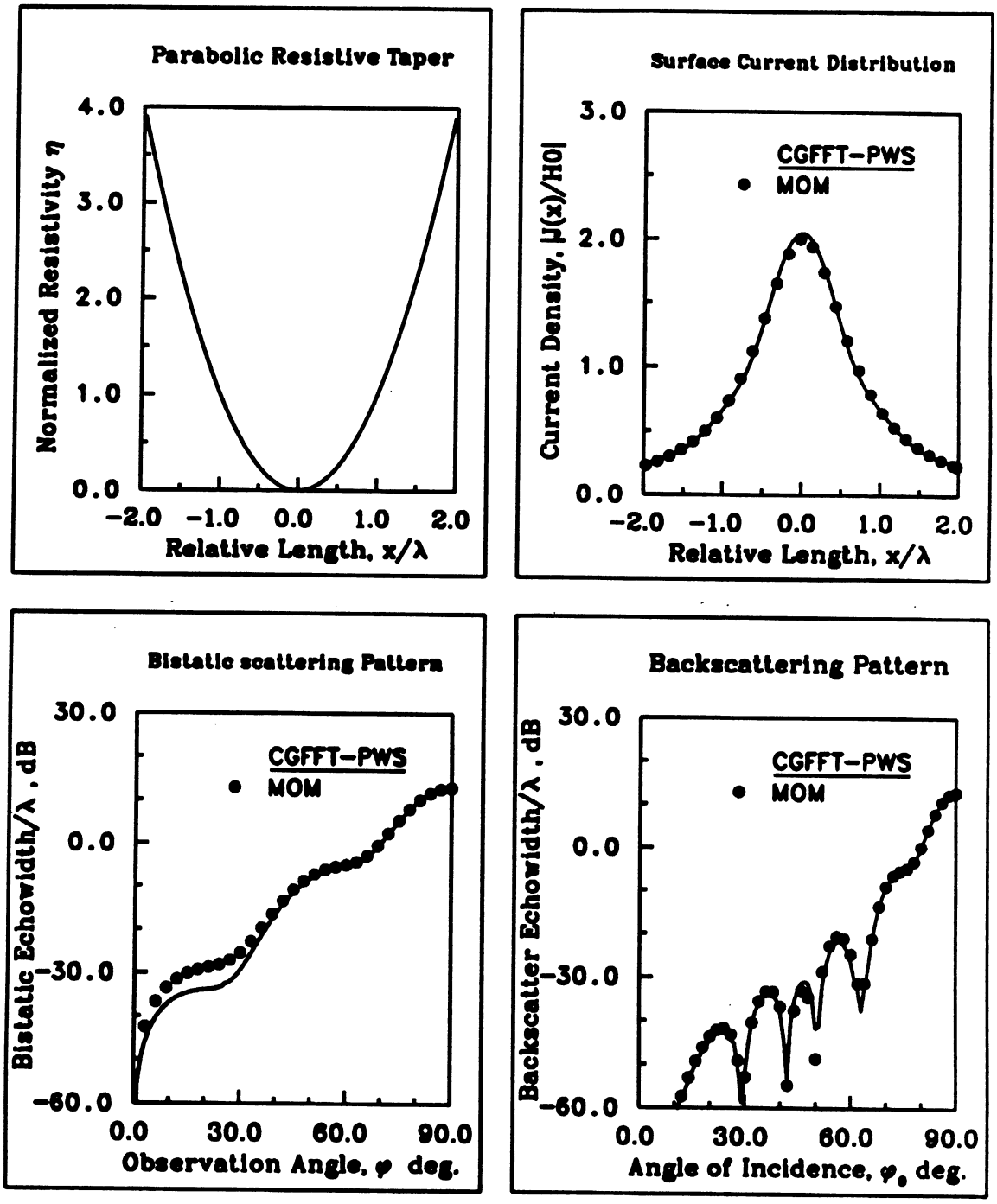

Figure 5.14: H-polarized scattering results for a 4λ parabolically tapered strip.

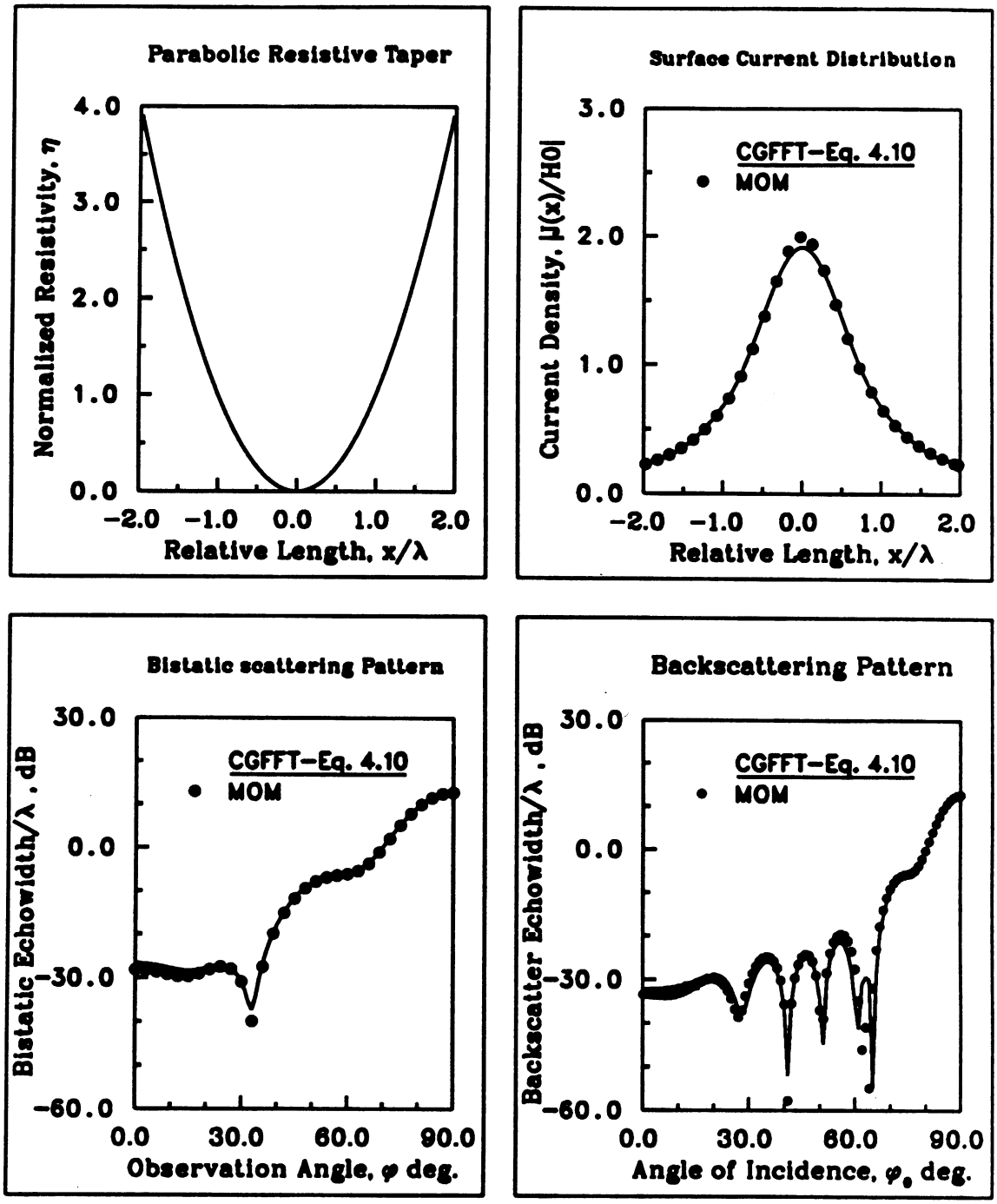

Figure 5.15: E-polarized scattering results for a 4λ parabolically tapered strip.

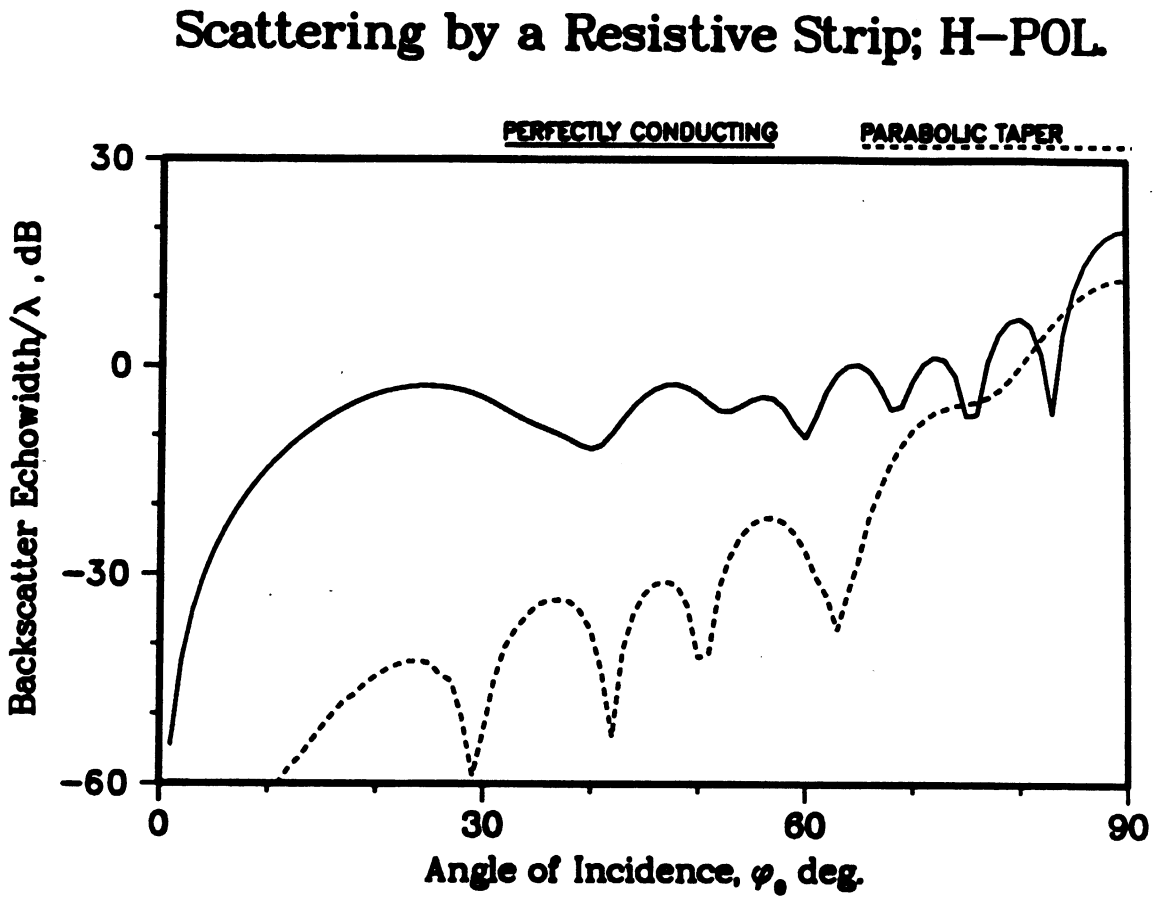

Figure 5.16: Comparison of the backscatter echowidths of a 4λ perfectly conducting and parabolically tapered strips for the H-polarization.

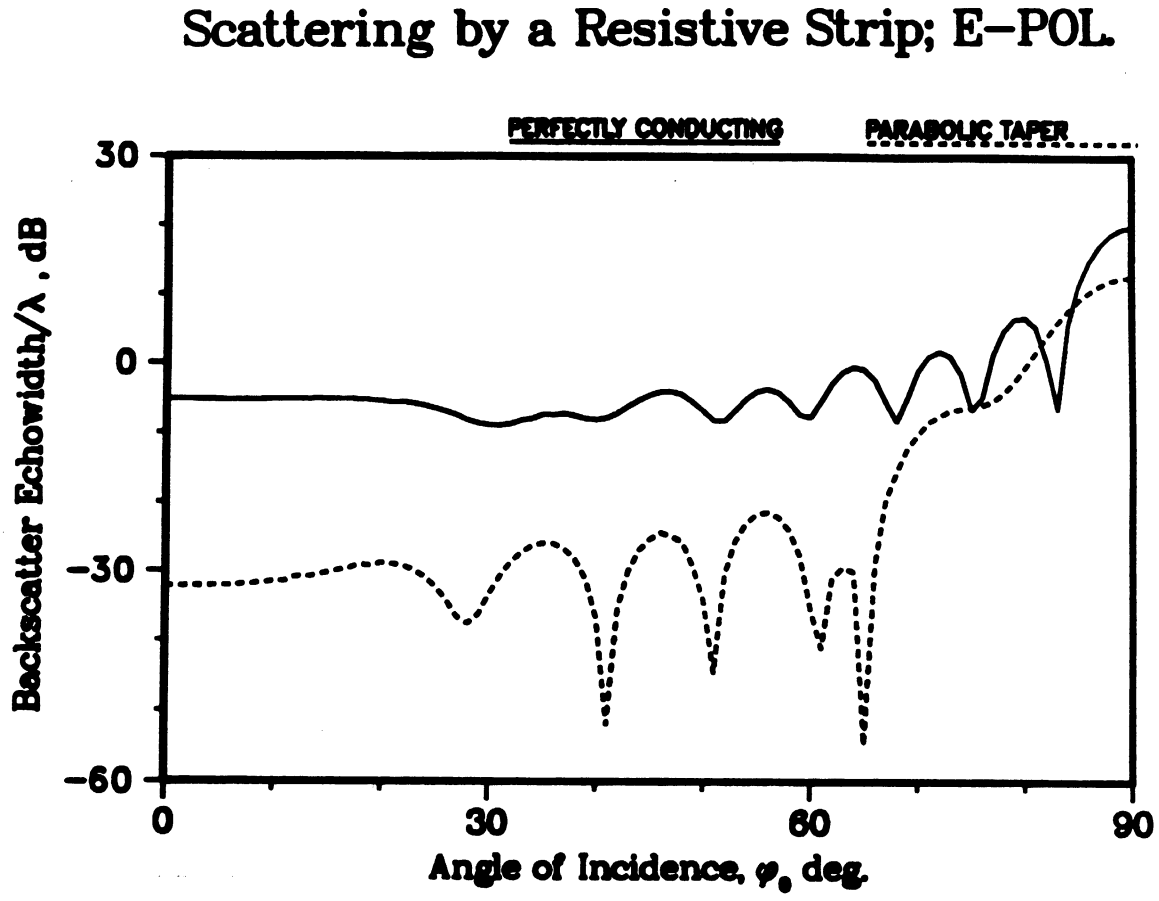

Figure 5.17: Comparison of the backscatter echowidths of a 4λ perfectly conducting and parabolically tapered strips for the E-polarization.

5.3 Scattering by a Dielectric Cylinder

Figure 5.18 shows the geometry for the case of scattering by a dielectric rectangular cylinder. The cylinder is assumed to be homogeneous, although the following formulation is equally applicable for inhomogeneous cylinders. Introducing the equivalent electric polarization current density[14] inside the cylinder

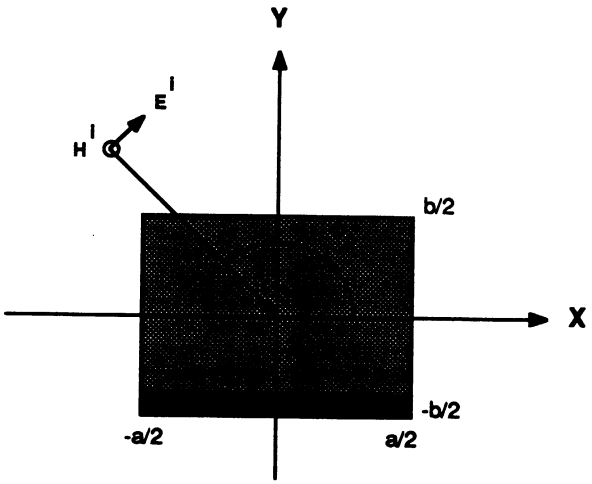

Figure 5.18: Geometry for a dielectric cylinder illuminated by a plane wave.

$$\mathbf{J}(\mathbf{r}) = j\omega(\epsilon - \epsilon_0)\mathbf{E}^{\mathbf{T}}, \tag{5.29}$$

the total electric field in the dielectric medium can be expressed as

$$\mathbf{E}^{\mathbf{T}} = \mathbf{E}^{\mathbf{i}} + \mathbf{E}^{\mathbf{s}} = \frac{Z_0}{j\omega(\epsilon_r - 1)}\mathbf{J} \cdot \tag{5.30}$$

The governing integral equations are subsequently obtained by substituting for the scattered field in (5.30). Thus, for E-polarization,

$$\mathbf{E}^{\mathbf{i}} = \hat{z}E_0 e^{jk_0\rho\ cos(\phi - \phi_0)} \tag{5.31}$$

$$\mathbf{J} = \hat{z} J_z(x,y) \tag{5.32}$$

and

$$H_0 e^{jk_0\rho\cos(\phi-\phi_0)} = \frac{1}{jk_0(\epsilon_r-1)} J_z(\rho) + \frac{k_0}{4}\int_{s'} J_z(\rho') H_0^{(2)}(k_0|\rho-\rho'|)ds' \tag{5.33}$$

where ρ and ϕ are the polar coordinates of the field point inside the cylinder and ϕ_0 is the angle of incidence. Similarly, for the H-polarization the corresponding equations are

$$\mathbf{H}^i = \hat{z} H_0 e^{jk_0\rho\cos(\phi-\phi_0)} \tag{5.34}$$

$$\mathbf{J} = \hat{x} J_x(x,y) + \hat{y} J_y(x,y) \tag{5.35}$$

and

$$\begin{aligned} H_0\sin(\phi_0)e^{jk_0\rho\cos(\phi-\phi_0)} &= \frac{1}{jk_0(\epsilon_r-1)} J_x(\rho) \\ &+\frac{1}{4k_0}\int_{s'}[J_x(k_0^2+\frac{\partial^2}{\partial x^2}) + J_y\frac{\partial^2}{\partial x\partial y}]H_0^{(2)}(k_0|\rho-\rho'|)ds' \end{aligned} \tag{5.36}$$

$$\begin{aligned} -H_0\cos(\phi_0)e^{jk_0\rho\cos(\phi-\phi_0)} &= \frac{1}{jk_0(\epsilon_r-1)} J_y(\rho) \\ &+\frac{1}{4k_0}\int_{s'}[J_x\frac{\partial^2}{\partial x\partial y} + J_y(k_0^2+\frac{\partial^2}{\partial y^2})]H_0^{(2)}(k_0|\rho-\rho'|)ds' \end{aligned} \tag{5.37}$$

which represent a system of coupled integral equations to be solved for J_x and J_y.

An implementation of the CGFFT formulation regarding (5.33) or (5.36) and (5.37) involves basis functions that are defined over a surface element, implying two dimensional Fourier transforms. Employing the known result[15]

$$\int_{-\infty}^{\infty} H_0^{(2)}(k_0\sqrt{x^2+y^2})e^{-jk_x x}dx = \frac{2}{\sqrt{k_0^2-k_x^2}} e^{-j|y|\sqrt{k_0^2-k_x^2}}, \tag{5.38}$$

the two dimensional Fourier transform of the Hankel function is calculated to be

$$\widetilde{H_0^{(2)}}(k_x,k_y) = \frac{4}{j(k_0^2-k_x^2-k_y^2)}. \tag{5.39}$$

The final operator equation can now be written for E-polarization as

$$\frac{E_z^i}{Z_0} = \frac{1}{jk_0(\epsilon_r - 1)} J_z(\rho) + \frac{1}{4k_0} \mathcal{F}^{-1}\{\widetilde{\mathcal{C}^e}\widehat{J_z}\} \tag{5.40}$$

where

$$\widetilde{\mathcal{C}^e} = k_0^2 \widetilde{H_0^{(2)}}(k_x, k_y)\tilde{f}(k_x, k_y)\cdot \tag{5.41}$$

Also, the corresponding system of equations for the H-polarization may be expressed in dyadic form as

$$\frac{\mathbf{E^i}}{Z_0} = \frac{1}{jk_0(\epsilon_r - 1)} \mathbf{J}(\rho) + \frac{1}{4k_0} \mathcal{F}^{-1}\{\widetilde{\bar{\mathcal{C}}^h} \cdot \hat{\mathbf{J}}\} \tag{5.42}$$

where

$$\widetilde{\bar{\mathcal{C}}^h} \equiv \begin{pmatrix} (k_0^2 - k_x^2)\widetilde{H_0^{(2)}}(k_x, k_y) & (-k_x k_y)\widetilde{H_0^{(2)}}(k_x, k_y) \\ (-k_x k_y)\widetilde{H_0^{(2)}}(k_x, k_y) & (k_0^2 - k_y^2)\widetilde{H_0^{(2)}}(k_x, k_y) \end{pmatrix} , \tag{5.43}$$

and

$$\tilde{\mathbf{J}}(k_x, k_y) = \begin{pmatrix} \tilde{f}(k_x, k_y)\hat{J}_x \\ \tilde{f}(k_x, k_y)\hat{J}_y \end{pmatrix} . \tag{5.44}$$

5.4 A Finite Material Plate

The case of a non-magnetic plate in the presence of an arbitrarily oriented short Hertzian dipole is considered next. The situation is depicted in figure 5.19.

Starting from the volume integral formulation for a layer, the boundary conditions involving tangential electric fields and normal electric flux are applied to the total field at the surface of the plate. Assuming no transverse variation for the current distribution across the plate, the thickness is forced to approach zero allowing the volume current to be replaced by equivalent surface current in the limit. The

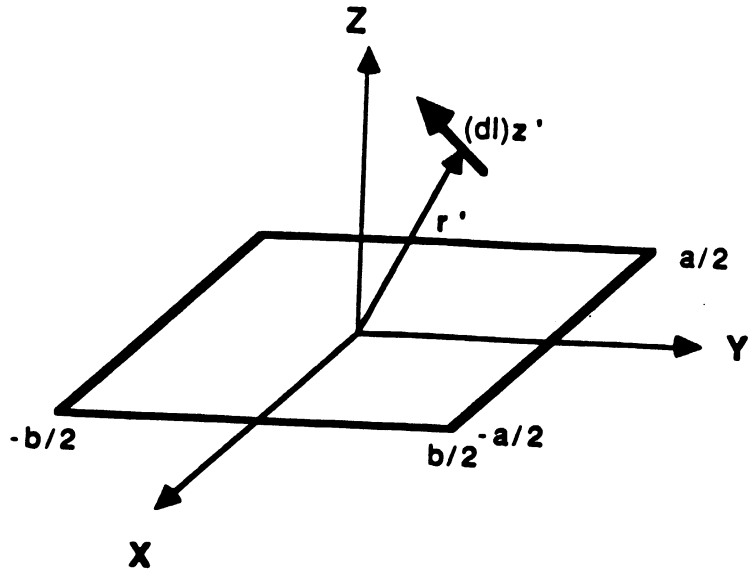

Figure 5.19: Geometry for a material plate in the presence of an arbitrarily oriented short Hertzian dipole.

plate is thus replaced by an equivalent composite sheet whose impedance is defined by the plate's electrical characteristics[16]. The relevant integro-differential equations for a homogeneous non-magnetic thin plate of relative permittivity ϵ_r and thickness τ are[8,16]

$$E_x^i(x,y) = R_x J_x(x,y) - [(k_0^2 + \frac{\partial^2}{\partial x^2})\Pi_x + \frac{\partial^2}{\partial x \partial y}\Pi_y] \tag{5.45}$$

$$E_y^i(x,y) = R_y J_y(x,y) - [\frac{\partial^2}{\partial x \partial y}\Pi_x + (k_0^2 + \frac{\partial^2}{\partial y^2})\Pi_y] \tag{5.46}$$

$$E_z^i(x,y) = R_z J_z(x,y) + [(\frac{\partial^2}{\partial x^2} + \frac{\partial^2}{\partial y^2})\Pi_z] \tag{5.47}$$

where $\mathbf{\Pi}$ is the electric Hertz vector defined in (5.3)

$$\mathbf{\Pi}(\mathbf{r}) = -\frac{jZ_0}{k_0}\int_{s'} \mathbf{J}(\mathbf{r}')G(\mathbf{r};\mathbf{r}')ds', \tag{5.48}$$

and G is the free space Green's function

$$G(\mathbf{r};\mathbf{r}') = \frac{e^{-jk_0|\mathbf{r}-\mathbf{r}'|}}{4\pi|\mathbf{r}-\mathbf{r}'|}. \tag{5.49}$$

Also,

$$R_x = R_y = \frac{-jZ_0}{k_0\tau(\epsilon_r - 1)}, \tag{5.50}$$

$$R_z = \frac{-j\epsilon_r Z_0}{k_0\tau(\epsilon_r - 1)}. \tag{5.51}$$

In the above, R_x and R_y are attributed to a resistive sheet supporting planar electric currents J_x and J_y, while R_z is attributed to a modified conductive sheet supporting planar magnetic currents represented by a sheet of vertical dipoles. It is noted that the two sheets are decoupled for the case of a planar plate considered.

Expanding the planar current components, J_x and J_y as in (4.11) and using the approximation (4.17) for the normal component of the current, the new system of integral equations suitable for the CGFFT method takes the form

$$\begin{aligned}
E_x^i(x,y) &= R_x J_x(x,y) + \frac{jZ_0}{k_0}\mathcal{F}^{-1}\{\tilde{G}(k_x,k_y)[(k_0^2 - k_x^2)\widetilde{J}_x(k_x,k_y) - k_x k_y \widetilde{J}_y(k_x,k_y)]\} \\
E_y^i(x,y) &= R_y J_y(x,y) + \frac{jZ_0}{k_0}\mathcal{F}^{-1}\{\tilde{G}(k_x,k_y)[-k_x k_y \widetilde{J}_x(k_x,k_y) + (k_0^2 - k_y^2)\widetilde{J}_y(k_x,k_y)]\} \\
E_z^i(x,y) &= R_z J_z(x,y) + \frac{jZ_0}{k_0}\mathcal{F}^{-1}\{\tilde{G}(k_x,k_y)(k_x^2 + k_y^2)\Delta s \widehat{J}_z\}
\end{aligned} \tag{5.52}$$

with $\hat{J}$ as defined before,

$$\widetilde{J}_x(k_x,k_y) = \tilde{f}(k_x,k_y)\widehat{J}_x(k_x,k_y) \tag{5.53}$$

$$\widetilde{J}_y(k_x,k_y) = \tilde{f}(k_x,k_y)\widehat{J}_y(k_x,k_y) \quad , \tag{5.54}$$

and

$$\tilde{G}(k_x,k_y) = \begin{cases} \frac{1}{2j\sqrt{k_0^2 - k_x^2 - k_y^2}} & , k_x^2 + k_y^2 < k_0^2 \\ \frac{1}{2\sqrt{k_x^2 + k_y^2 - k_0^2}} & , k_x^2 + k_y^2 > k_0^2 \end{cases} . \tag{5.55}$$

However, since the piecewise sinusoidal basis function $S(x,y)$ given in (4.14) vanishes at the end-points, it does not provide an accurate representation for the

current density flowing parallel to the plate's edges where it is non-zero. A similar situation arises in the analysis of the conducting strip illuminated by an E-polarized plane wave. Therefore, it is necessary that corrective measures be employed when using this basis function for such problems. Below, a method is presented to partially alleviate this difficulty as applied to the rectangular plate geometry and a similar procedure is suitable for the one dimensional case.

Each component of the current density is expressed using sinusoidal expansion functions so that the basis elements associated with the current component perpendicular to the edges go to zero. Meanwhile, those corresponding to the component parallel to the edges are extended to include an additional set of subsectional expansion functions which are non-zero at the edges as shown by dotted lines in figure 5.20. The final current representation is subsequently obtained by subtracting out

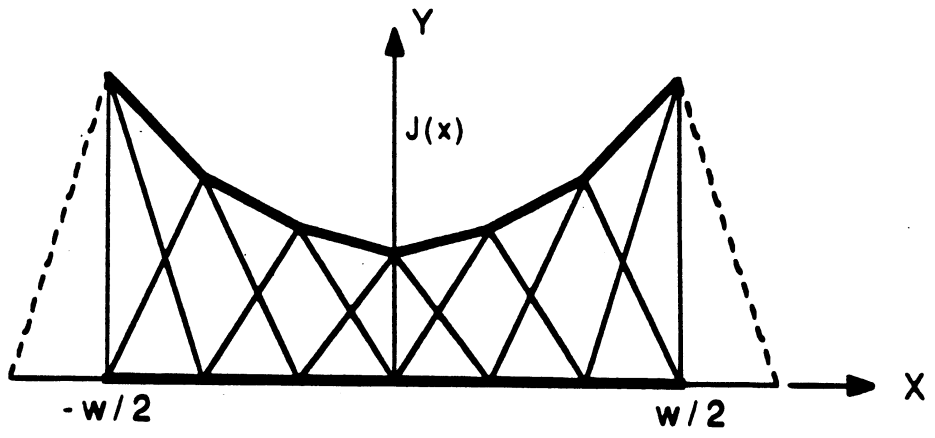

Figure 5.20: The extended sinusoidal basis functions for the current component which is nonzero at the edge.

the portion of the basis element that extends beyond the plate. As a result, the Fourier transforms of the planar components of the current can now be written as

$$\tilde{J}_x(k_x,k_y) = \tilde{S}(k_x,k_y)\hat{J}_x(k_x,k_y) - \tilde{S}(k_x)\Omega_x(k_y) \quad (5.56)$$

$$\tilde{J}_y(k_x,k_y) = \tilde{S}(k_x,k_y)\hat{J}_y(k_x,k_y) - \tilde{S}(k_y)\Omega_y(k_x) \quad , \quad (5.57)$$

where Ω_x and Ω_y account for the contribution of the extraneous current elements introduced outside the plate. They are given by

$$\Omega_x(k_y) = J_x(x,-b/2)\chi^-(k_y) + J_x(x,b/2)\chi^+(k_y) \quad (5.58)$$

$$\Omega_y(k_x) = J_y(-a/2,y)\chi^-(k_x) + J_y(a/2,y)\chi^+(k_x) \quad (5.59)$$

where χ^- and χ^+ denote the Fourier transforms of the shifted right and left halves of the sinusoidal basis function. For the y component they are given by

$$\chi^+(k_x) = \tilde{S}^+(k_x)e^{-jk_x\frac{a}{2}} \quad (5.60)$$

$$\chi^-(k_x) = \tilde{S}^-(k_x)e^{jk_x\frac{a}{2}} \quad (5.61)$$

where

$$\tilde{S}^+(k_x) = \frac{1}{j\sin(k_0\Delta x)}\{e^{j[(k_0-k_x)\frac{\Delta x}{2}]}\frac{\sin[(k_0+k_x)\frac{\Delta x}{2}]}{k_0+k_x} - e^{-j[(k_0+k_x)\frac{\Delta x}{2}]}\frac{\sin[(k_0-k_x)\frac{\Delta x}{2}]}{k_0-k_x}\}$$

$$\tilde{S}^-(k_x) = \frac{1}{j\sin(k_0\Delta x)}\{e^{j[(k_0+k_x)\frac{\Delta x}{2}]}\frac{\sin[(k_0-k_x)\frac{\Delta x}{2}]}{k_0-k_x} - e^{-j[(k_0-k_x)\frac{\Delta x}{2}]}\frac{\sin[(k_0+k_x)\frac{\Delta x}{2}]}{k_0+k_x}\}. \quad (5.62)$$

With these modifications, equations (5.52) can be formally written as

$$A[\mathbf{J}] = \bar{\mathbf{R}}\cdot\mathbf{J} + \frac{jZ_0}{k_0}\mathcal{F}^{-1}\{\tilde{\bar{\mathcal{D}}}\cdot\tilde{\mathbf{J}}\} = \mathbf{E}^{\mathbf{i}} \quad (5.63)$$

where

$$\tilde{\bar{\mathcal{D}}} \equiv \begin{pmatrix} (k_0^2 - k_x^2)\tilde{G} & (-k_x k_y)\tilde{G} & 0 \\ (-k_x k_y)\tilde{G} & (k_0^2 - k_y^2)\tilde{G} & 0 \\ 0 & 0 & (k_x^2 + k_y^2)\tilde{G} \end{pmatrix} , \tag{5.64}$$

$$\bar{\mathbf{R}} = \begin{pmatrix} R_x & 0 & 0 \\ 0 & R_y & 0 \\ 0 & 0 & R_z \end{pmatrix} , \tag{5.65}$$

and

$$\tilde{\mathbf{J}}(k_x, k_y) = \begin{pmatrix} \tilde{S}(k_x)[\tilde{S}(k_y)\hat{J}_x - \Omega_x(k_y)] \\ \tilde{S}(k_y)[\tilde{S}(k_x)\hat{J}_y - \Omega_y(k_x)] \\ \Delta s \hat{J}_z \end{pmatrix} . \tag{5.66}$$

The above formulation was applied to plates of various sizes and compositions. Figures 5.21 and 5.22 show the planar current densities for a $1\lambda \times 1\lambda$ conducting plate illuminated with a horizontally oriented Hertzian dipole located 0.25λ above the center of the plate. A principal plane normalized radiation pattern(appendix D) for this geometry is shown in figure 5.23 along with the corresponding result obtained via the MOM[17]. Clearly, the agreement between the two solutions verifies that the CGFFT has converged to the correct solution. Also, shown in figure 5.24 is the improvement in the rate of convergence when the piecewise sinusoidal is used. The results for the same plate when the dipole is oriented vertically are given in figures 5.25 to 5.30. Due to the symmetry of the problem in this case, the two current components are identical except for a $\pi/2$ shift in the distribution(Fig. 5.25 and 5.26). Also, it is observed that the spectra of the planar currents do not identically go to zero at the edges parallel to the component under consideration

as shown in figure 5.27 for the J_x component. This is in agreement with the edge condition as discussed elsewhere in this report.

The formulation was applied to larger plates as well. In all cases the usual improvement in the convergence rate of the solution was observed when the sinusoidal basis functions were used. For example, the convergence patterns for $2\lambda \times 2\lambda$ and $5\lambda \times 5\lambda$ conducting plates are shown in figures 5.31 and 5.32, respectively. The plates are illuminated with a horizontal Hertzian dipole. The excited surface current densities on a thin $5\lambda \times 2\lambda$ dielectric plate($\epsilon' = 4.$) in the presence of a vertical Hertzian dipole are given in figures 5.33 and 5.34. It is noted that since the edge currents are no longer dominant, the convergence was achieved after only 6 iterations using the extended PWS basis functions.

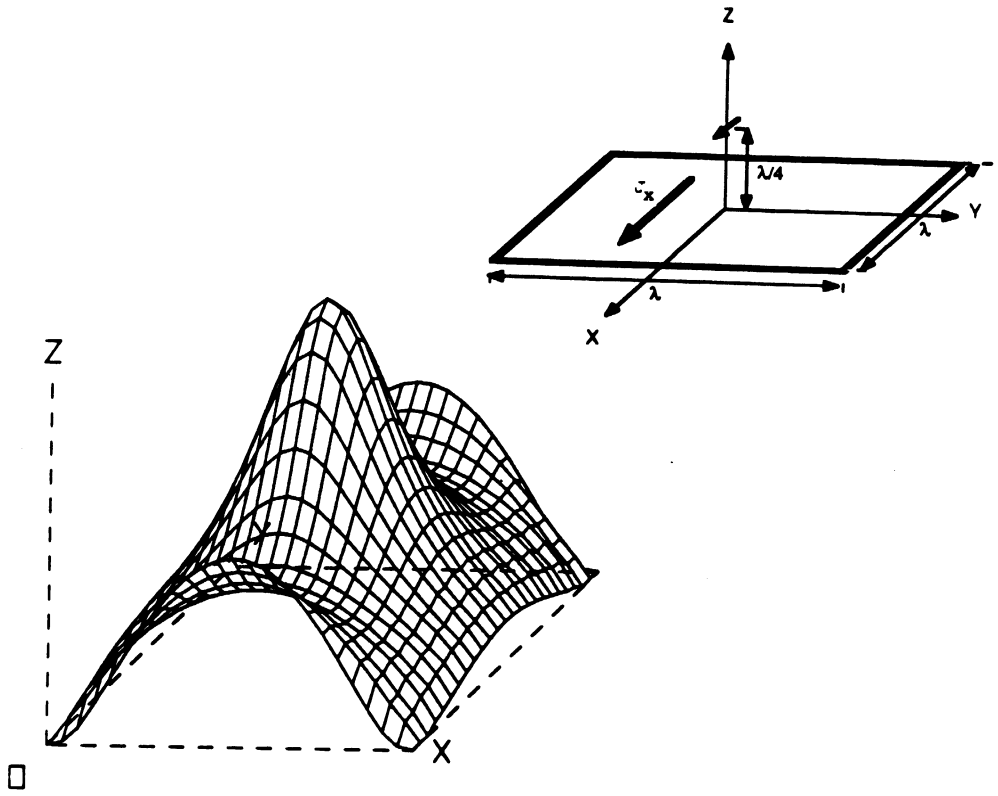

Figure 5.21: The like-polarized component of the surface current density on a $1\lambda \times 1\lambda$ conducting plate irradiated by a horizontal Hertzian dipole positioned $\lambda/4$ above the center of the plate(25×25 unknowns and FFT pad of order 2).

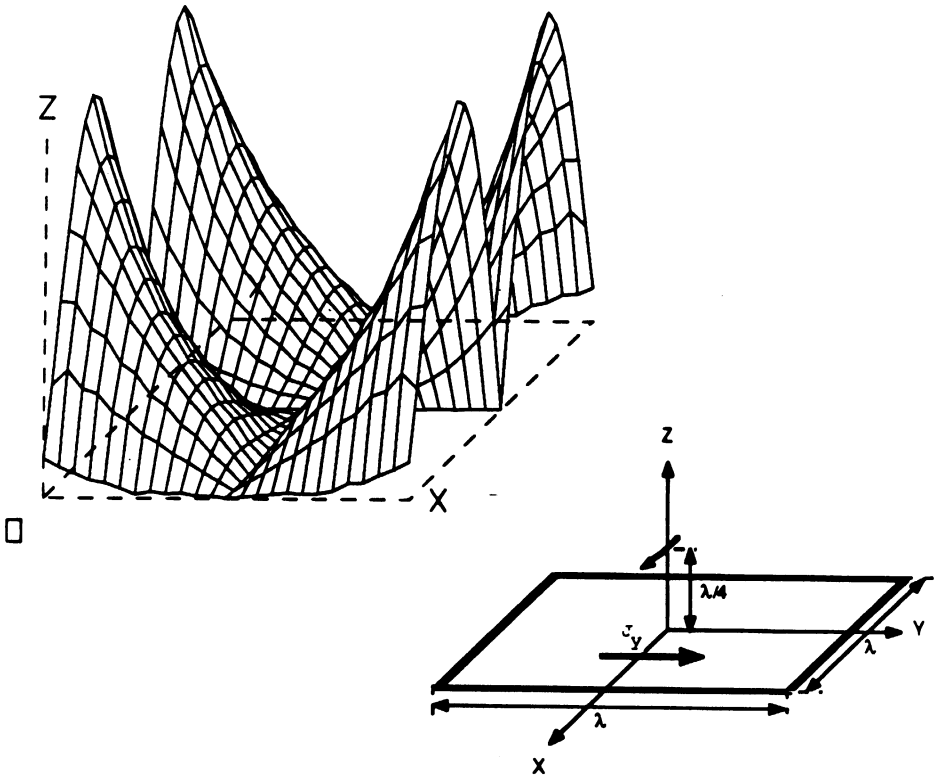

Figure 5.22: The cross-polarized component of the surface current density on a $1\lambda \times 1\lambda$ conducting plate irradiated by a horizontal Hertzian dipole positioned $\lambda/4$ above the center of the plate(25×25 unknowns and FFT pad of order 2).

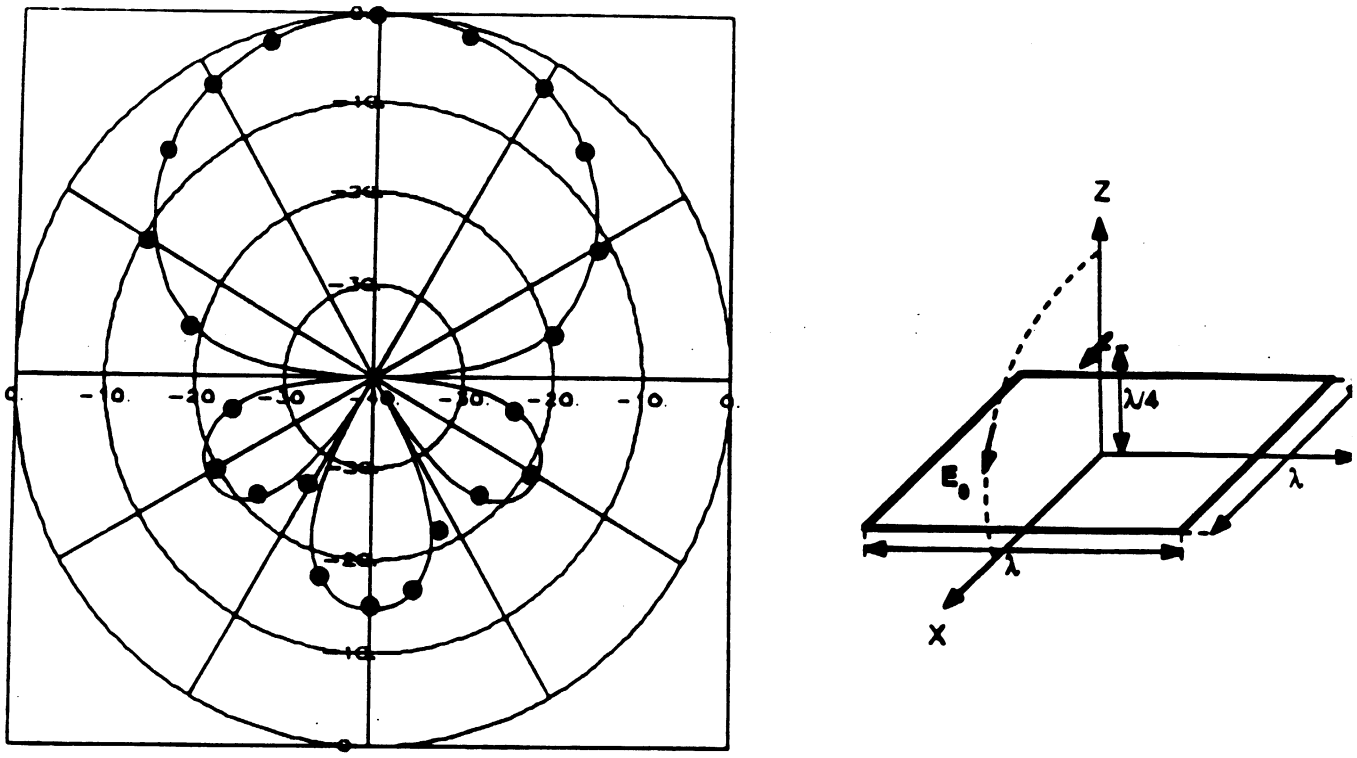

Figure 5.23: Principal plane radiation pattern($E_\theta(\theta, \phi = 0)$) of a short horizontal Hertzian dipole in the presence of a $1\lambda \times 1\lambda$ conducting plate computed by the MOM and the CGFFT using extended sinusoidal basis functions.

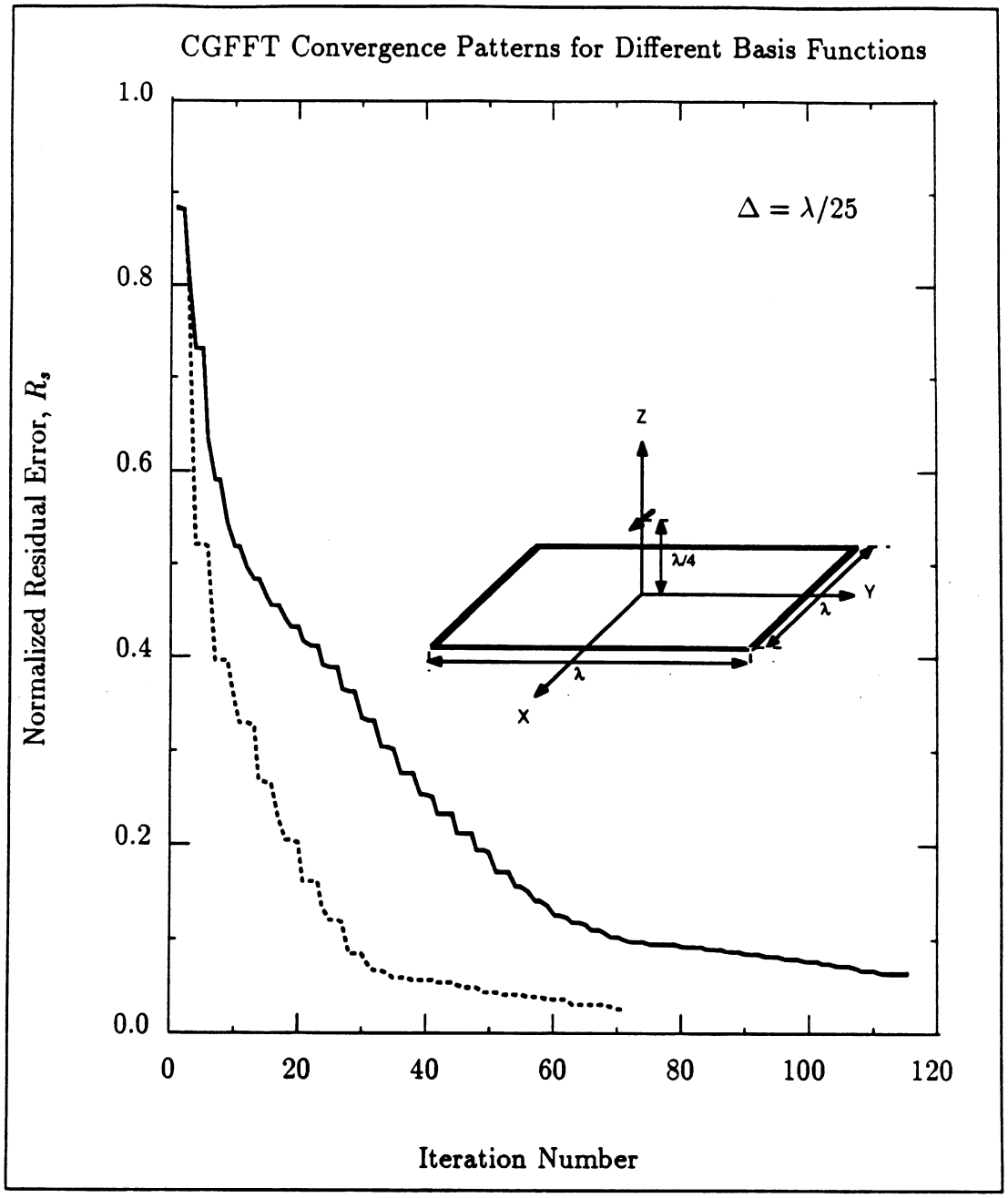

Figure 5.24: Convergence rate of the normalized residual error pertinent to the radiation of a horizontal Hertzian dipole in the presence of a $1\lambda \times 1\lambda$ flat conducting plate.(Solid line: approximate eq. 4.17; dashed line: extended PWS.)

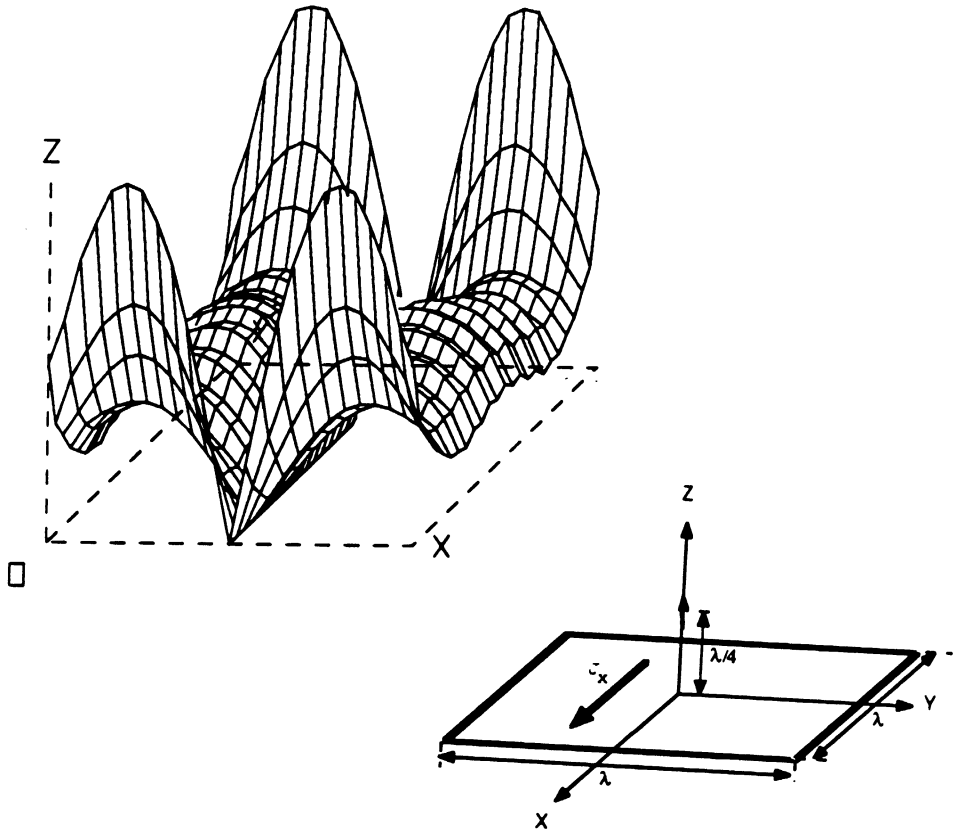

Figure 5.25: The X-component of the surface current density on a $1\lambda \times 1\lambda$ conducting plate irradiated by a vertical Hertzian dipole positioned $\lambda/4$ above the center of the plate(25×25 unknowns and FFT pad of order 2).

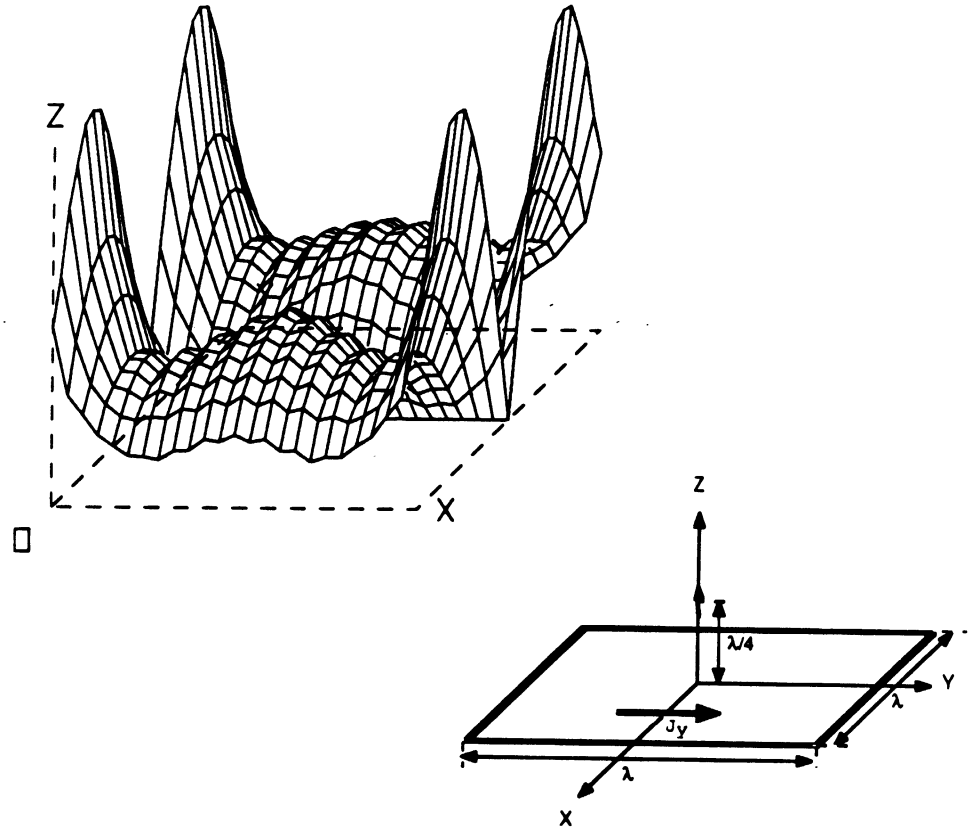

Figure 5.26: The Y-component of the surface current density on a $1\lambda \times 1\lambda$ conducting plate irradiated by a vertical Hertzian dipole positioned $\lambda/4$ above the center of the plate(25×25 unknowns and FFT pad of order 2).

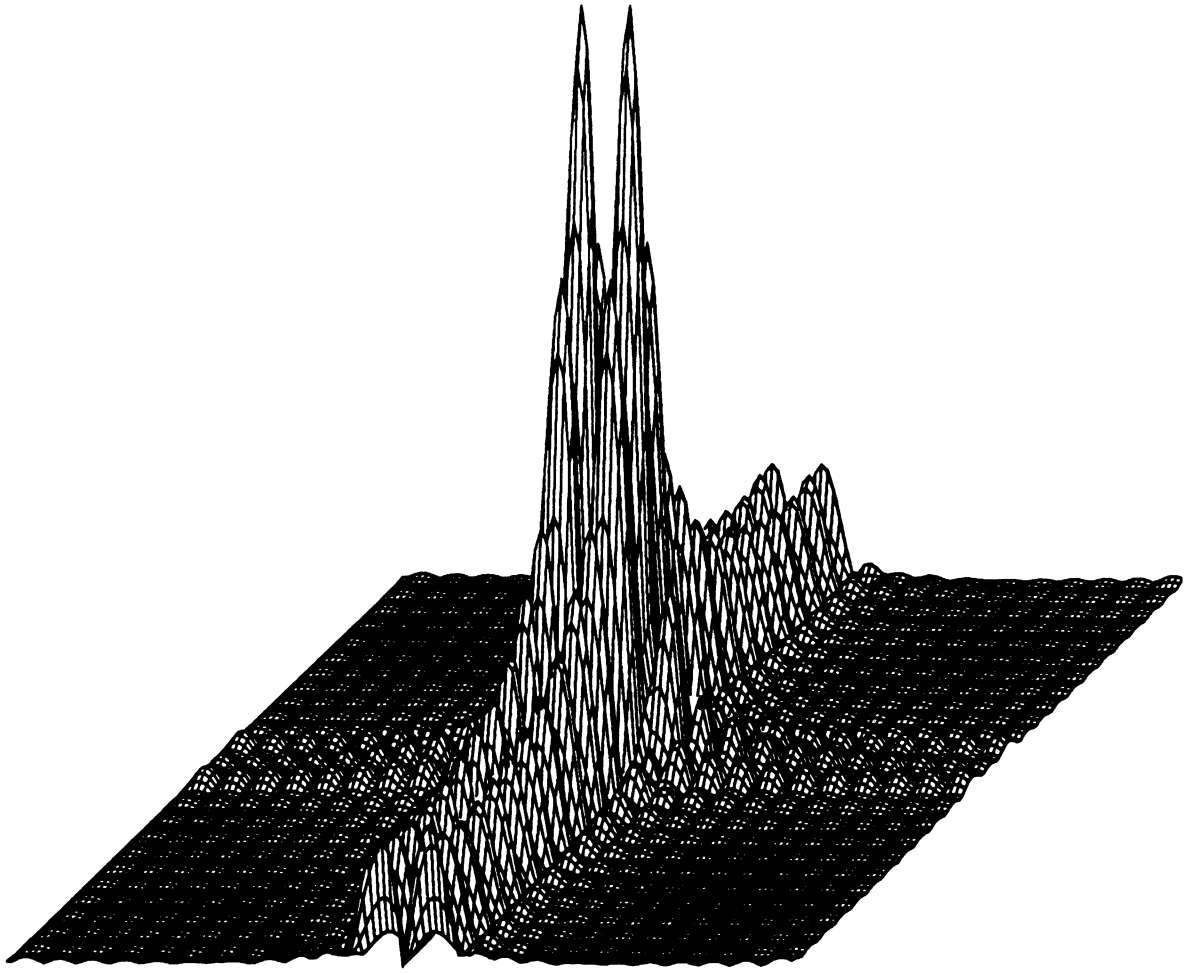

Figure 5.27: The spectrum of the surface current density(X-component) for the $1\lambda \times 1\lambda$ conducting plate irradiated by a vertical Hertzian dipole positioned $\lambda/4$ above the center of the plate(25×25 unknowns and FFT pad of order 2).

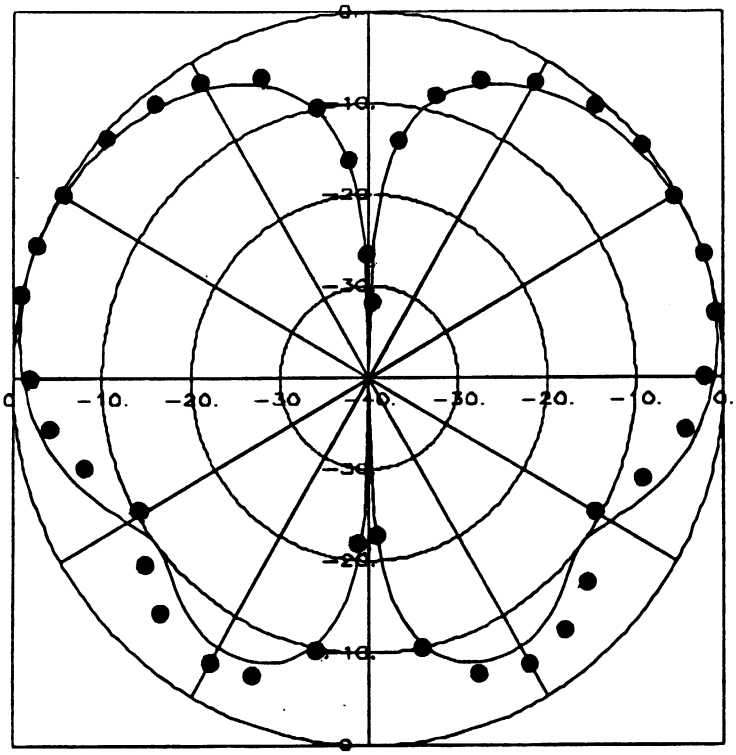

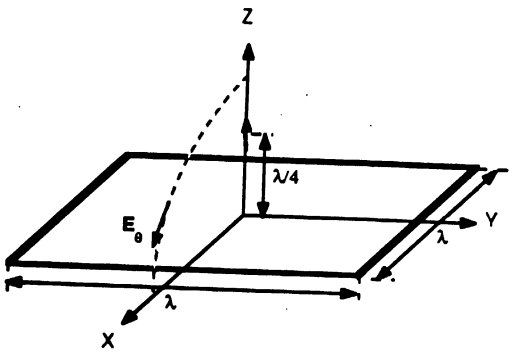

Figure 5.28: Principal plane radiation pattern($E_\theta(\theta, \phi = 0)$) of a short vertical Hertzian dipole in the presence of a $1\lambda \times 1\lambda$ conducting plate computed by the MOM and the CGFFT using extended sinusoidal basis functions.

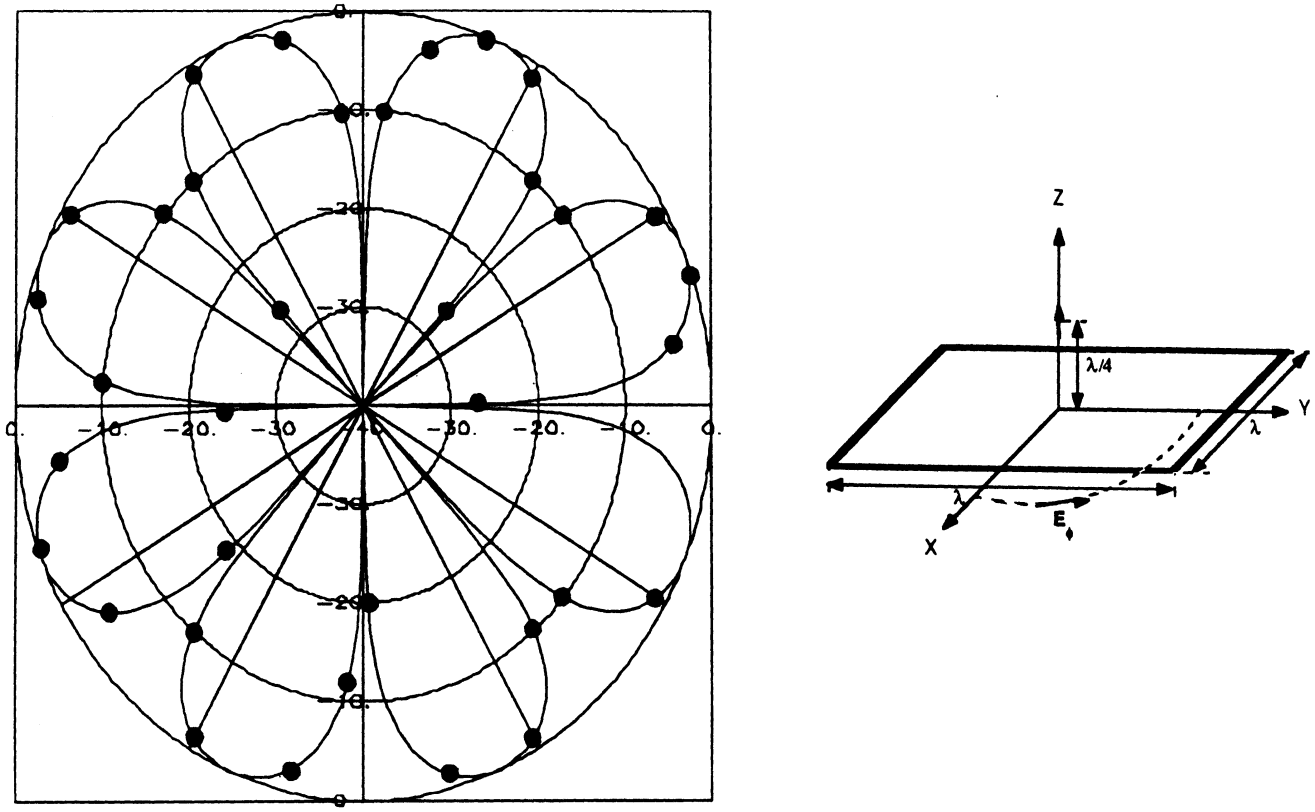

Figure 5.29: Principal plane radiation pattern($E_\phi(\theta = \frac{\pi}{2}, \phi)$) of a short vertical Hertzian dipole in the presence of a $1\lambda \times 1\lambda$ conducting plate computed by the MOM and the CGFFT using extended sinusoidal basis functions.

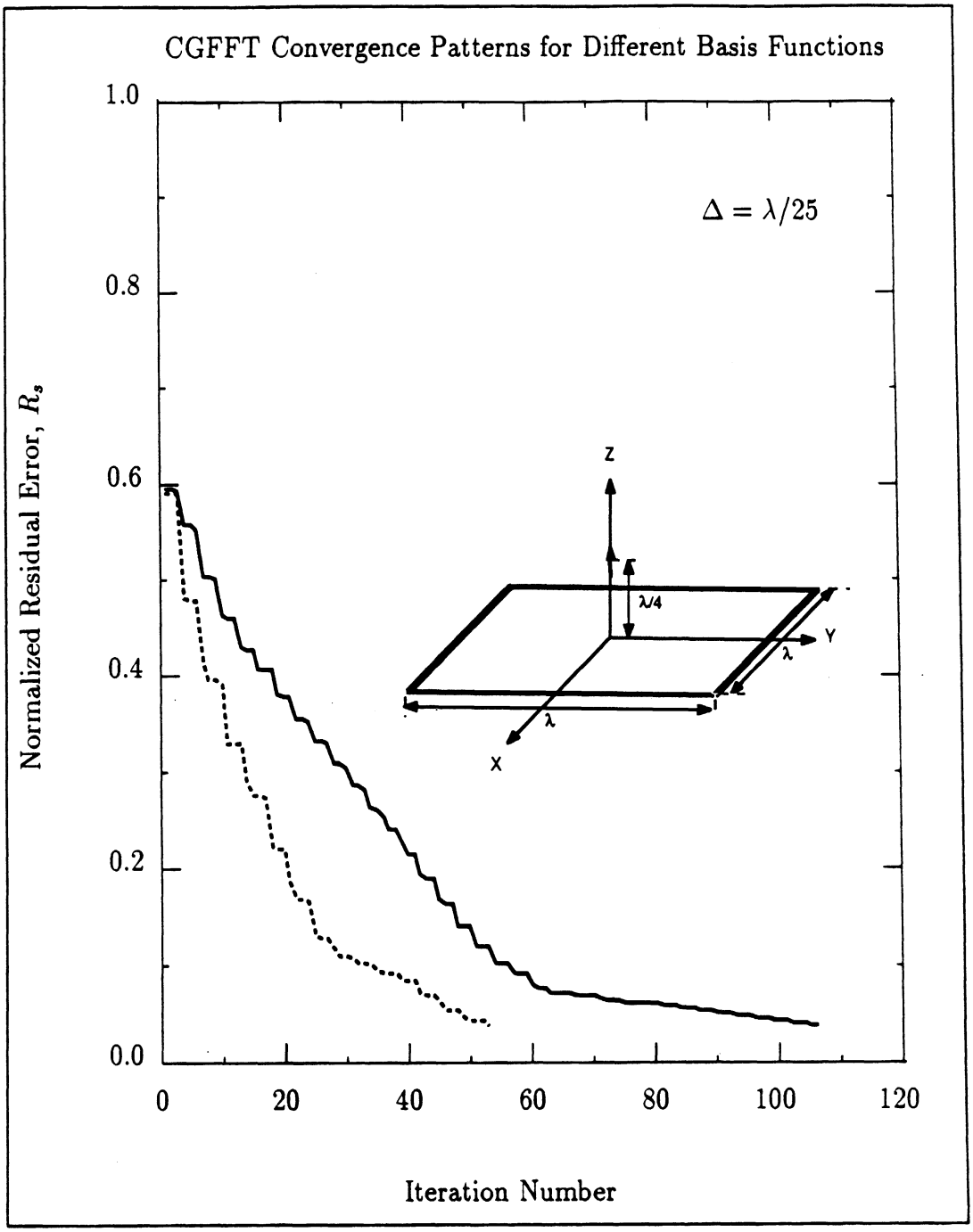

Figure 5.30: Convergence rate of the normalized residual error pertinent to the radiation of a vertical Hertzian dipole in the presence of a $1\lambda \times 1\lambda$ flat conducting plate.(Solid line: approximate eq. 4.17; dashed line: extended PWS.)

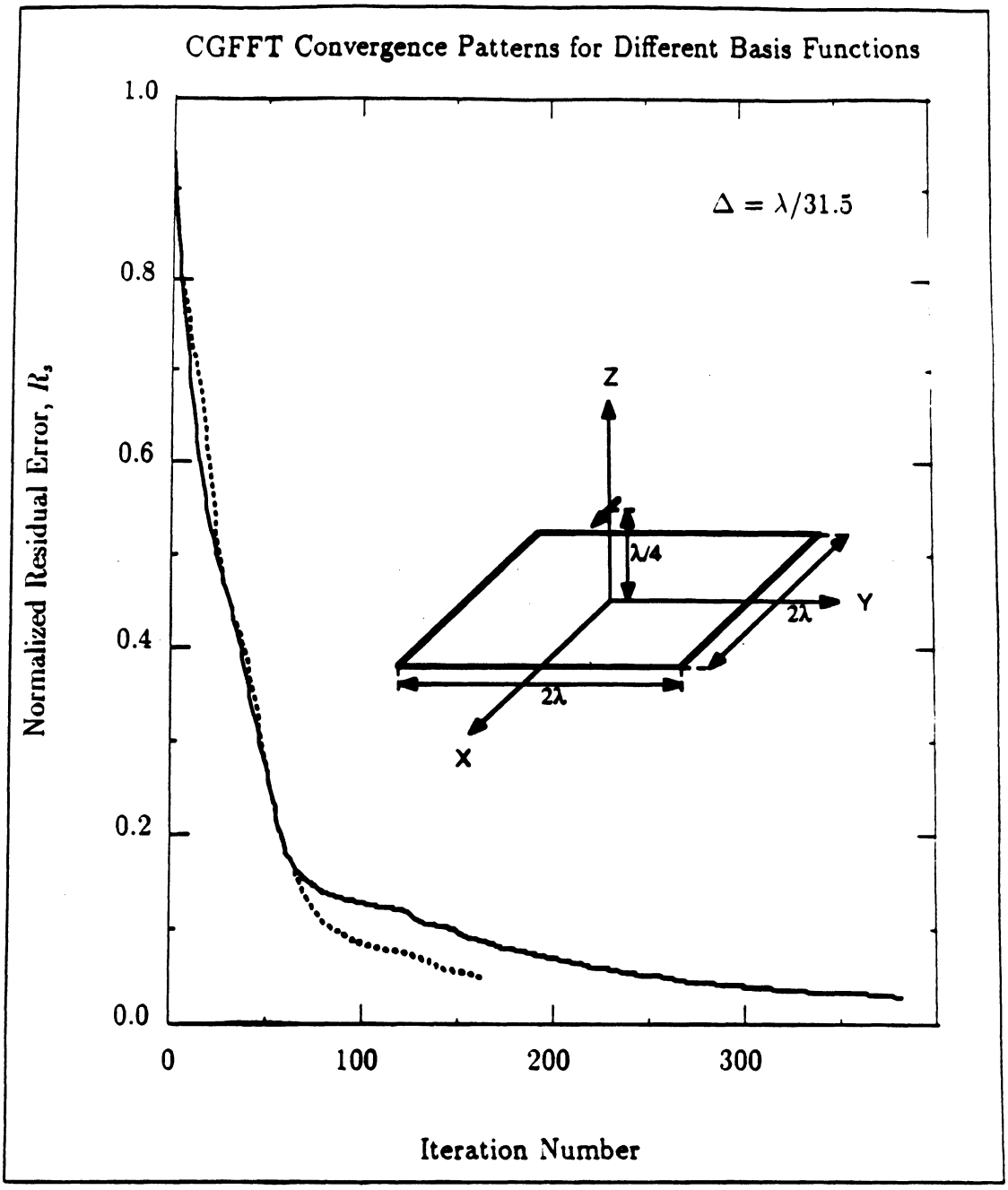

Figure 5.31: Convergence rate of the normalized residual error pertinent to the radiation of a horizontal Hertzian dipole in the presence of a $2\lambda \times 2\lambda$ flat conducting plate.(Solid line: approximate eq. 4.17; dashed line: extended PWS.)

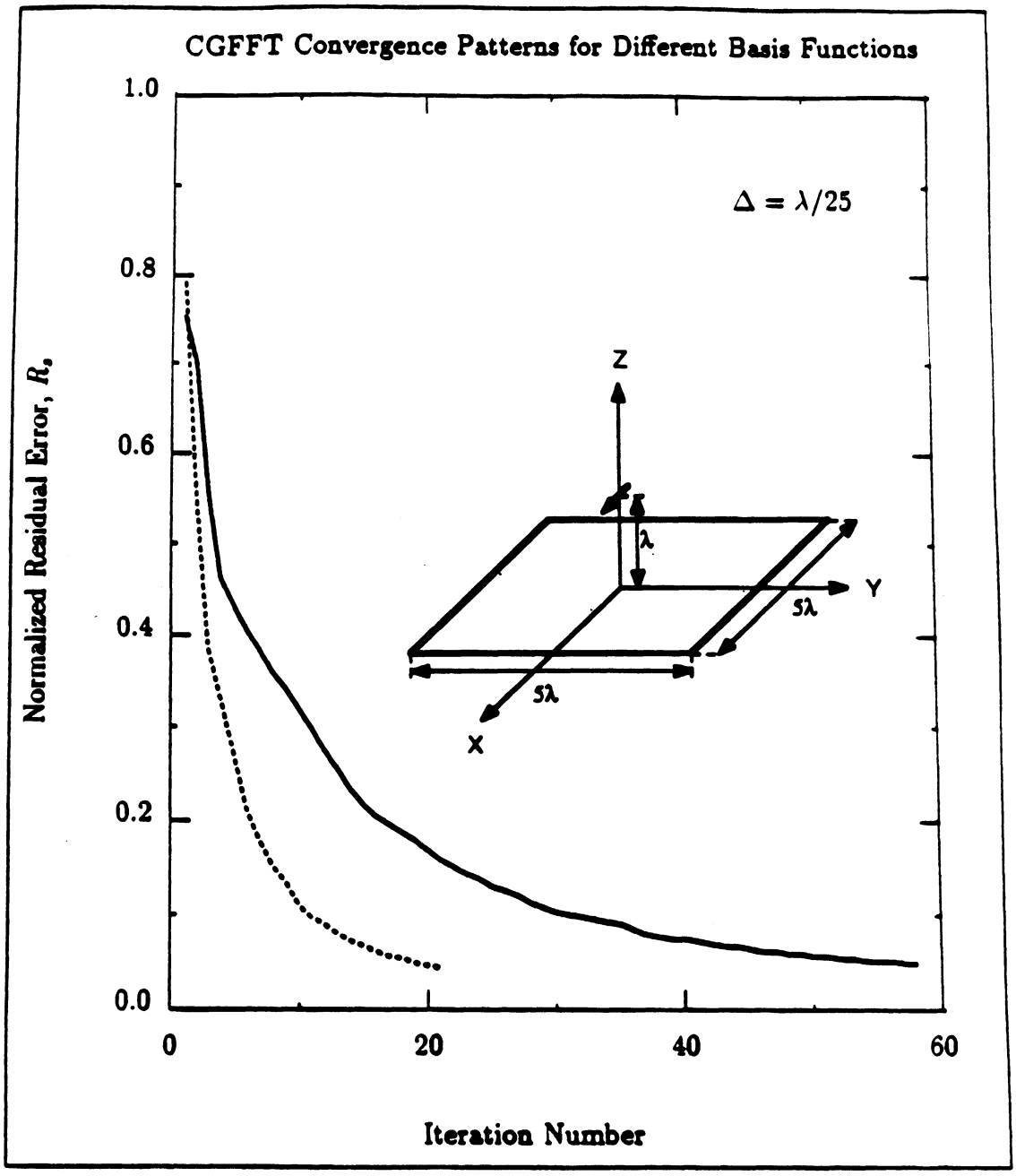

Figure 5.32: Convergence rate of the normalized residual error pertinent to the radiation of a horizontal Hertzian dipole in the presence of a $5\lambda \times 5\lambda$ flat conducting plate.(Solid line: approximate eq. 4.17; dashed line: extended PWS.)

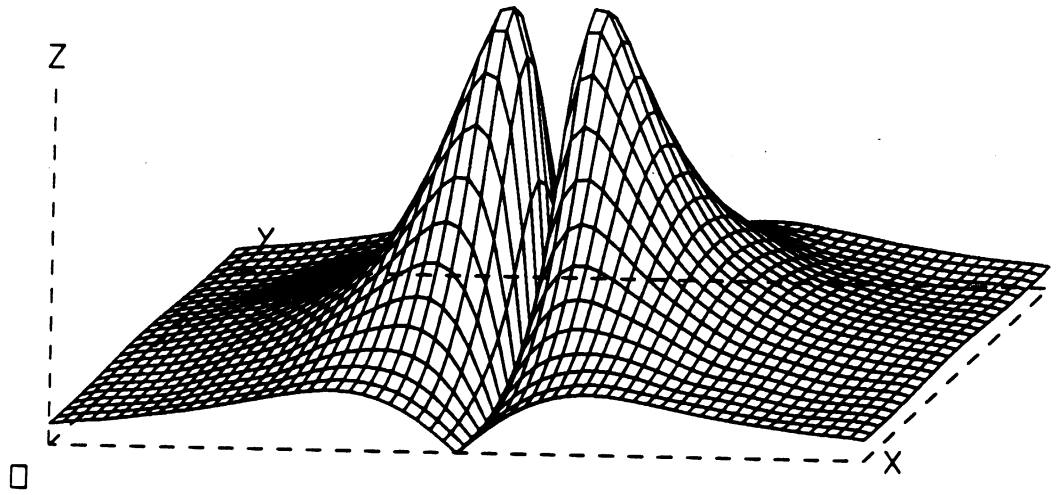

Figure 5.33: The X-component of the excited surface current density on a $5\lambda \times 2\lambda$ dielectric plate irradiated by a vertical Hertzian dipole(12×12 unknowns/λ^2.)

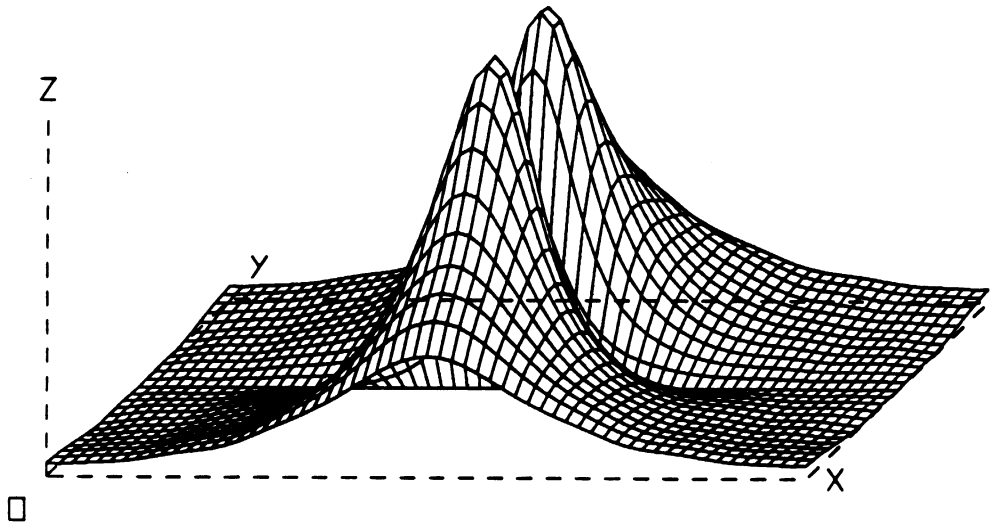

Figure 5.34: The Y-component of the excited surface current density on a $5\lambda \times 2\lambda$ dielectric plate irradiated by a vertical Hertzian dipole.(12×12 unknowns/λ^2.)

Chapter 6

Concluding Remarks

The application of the conjugate gradient FFT method to antenna and scattering problems was explored. A technique was presented to improve the convergence of the conjugate gradient FFT method by introducing subdomain basis functions in the formulation of the problem. The CGFFT formulation was thus extended to generalized expansion functions. It was shown through several examples that this formulation can be efficiently utilized in the analysis of large systems. In particular, for the problems investigated in this study, the rate of convergence was shown to increase by a factor of two when incorporating sinusoidal basis functions. The improvement in the rate of convergence is attributed to a more accurate representation of the current in the spectral domain.

A faster convergence rate translates into a shorter CPU processing time as depicted in figure 6.1 for the case of a 1λ dipole.

Finally, to evaluate the performance of the CGFFT method, the storage requirements and the total number of operations for the CGFFT and the Gaussian elimination are listed in table 6.1. The storage constraints for the two methods

Method	Storage Requirement†	No. of Operations‡
Direct	$N^2 + 3N$	$2N^3/3 + 3N^2/2 - N/6$
CGFFT	$6N + N' + 3$	$(4N' \log_2 N' + 10N + 2) \times N_i$

†,‡ N = No. of unknowns, $N' = 2^{\{INT[\log_2(2N-1)]+\rho\}}$, N_i = No. of iterations.

Table 6.1: Comparison between the performances of the Gaussian elimination and the CGFFT methods.

are plotted in figure 6.2. Clearly, the CGFFT method offers a substantial storage economy over the direct method which requires prohibitive storage sizes ,in terms of computer memory, for large problems. Figure 6.3 compares the performance of the two methods based on the entries in the second column of table 6.1. Here the equivalent number of iterations is plotted versus the number of unknowns. For a given number of unknowns, the solid line gives the upper limit on the number of iterations allowed for the CGFFT in order for the method to match the speed of the corresponding direct algorithm. On the other hand, it is known from the theory of the the conjugate directions- and from numerical experiments with CGFFT- that the number of iterations required for the method to achieve a reasonably small tolerance is always less than the corresponding number of unknowns(the bound indicated by the dashed line). Thus, it is concluded that for the problems whose sizes exceed a certain limit, the CGFFT is actually faster than the corresponding direct method. This is indeed the case as shown in figure 6.4 where the CPU times needed to solve for the current distribution on a resonant dipole are plotted versus the number of unknowns using the two methods. All computations were

carried out on an Apollo DN 3000 node. As it can be seen from the figure, for larger problems the conjugate gradient FFT method becomes more efficient than the direct Gaussian elimination. The speed is further improved when CGFFT is applied in conjunction with piecewise sinusoidal expansion functions, as discussed before. Also shown in figure 6.4, is the impressive performance of the special moment method algorithm for the solution of purely Toeplitz matrices. Although this algorithm takes full advantage of the structural symmetries of such problems, it is not applicable when the diagonal elements of the system matrix are no longer identical(perturbed Toeplitz) as in the case of scattering from an inhomogeneous structure. For such cases, however, the CGFFT formulation discussed in this report remains valid and is applicable because the convolutional nature of the integral operator is not disturbed by the inhomogeneouities.

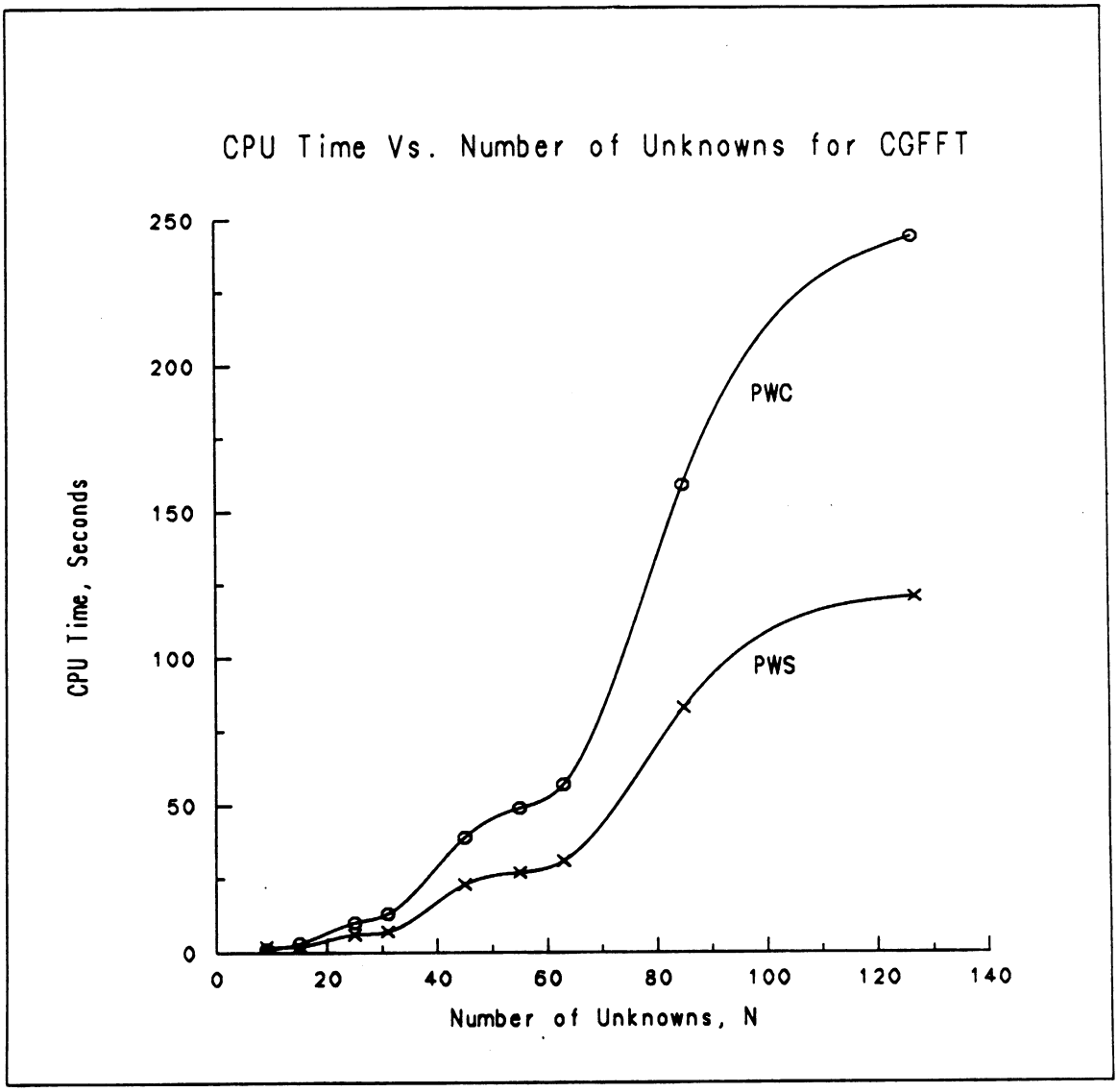

Figure 6.1: The improvement in the CPU time for the problem of a 1λ wire dipole($a = .005\lambda$) as a function of the number of unknowns.

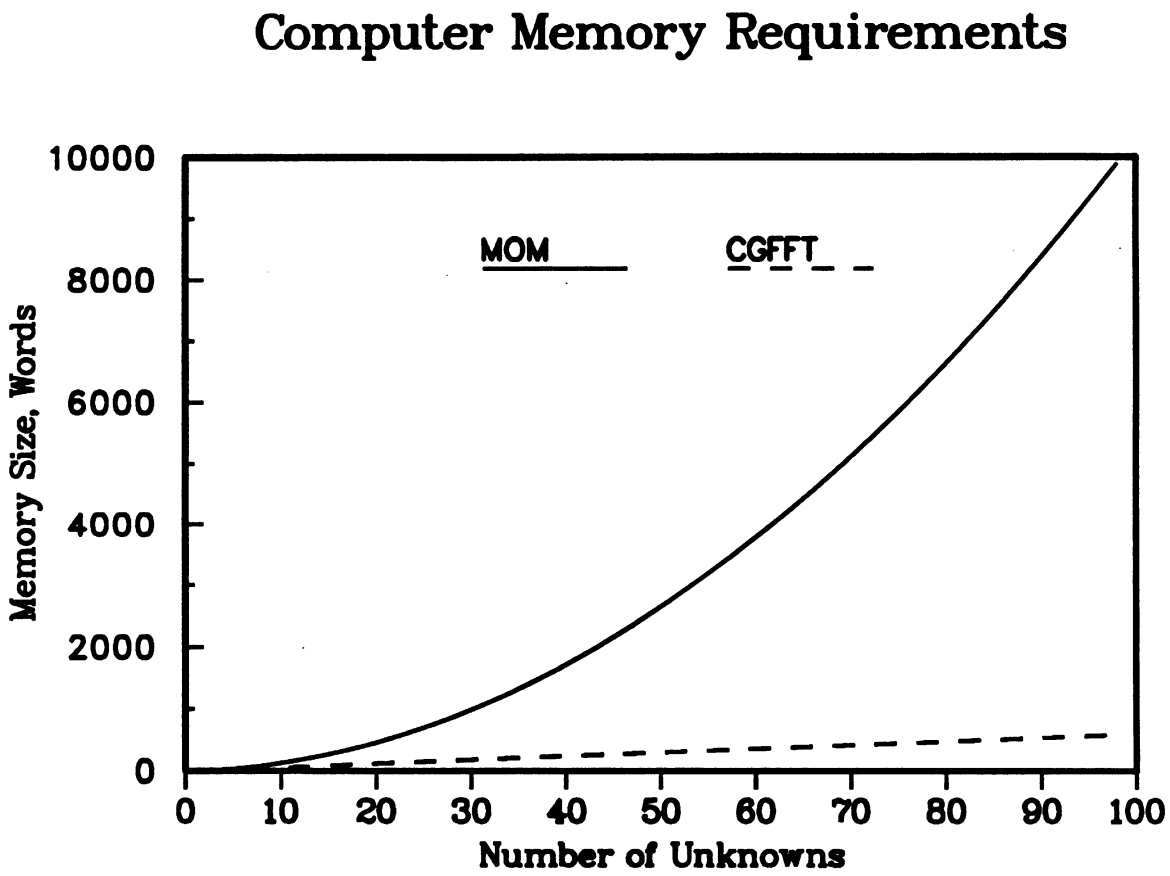

Figure 6.2: The storage requirement of the MOM and the CGFFT based on table 6.1.

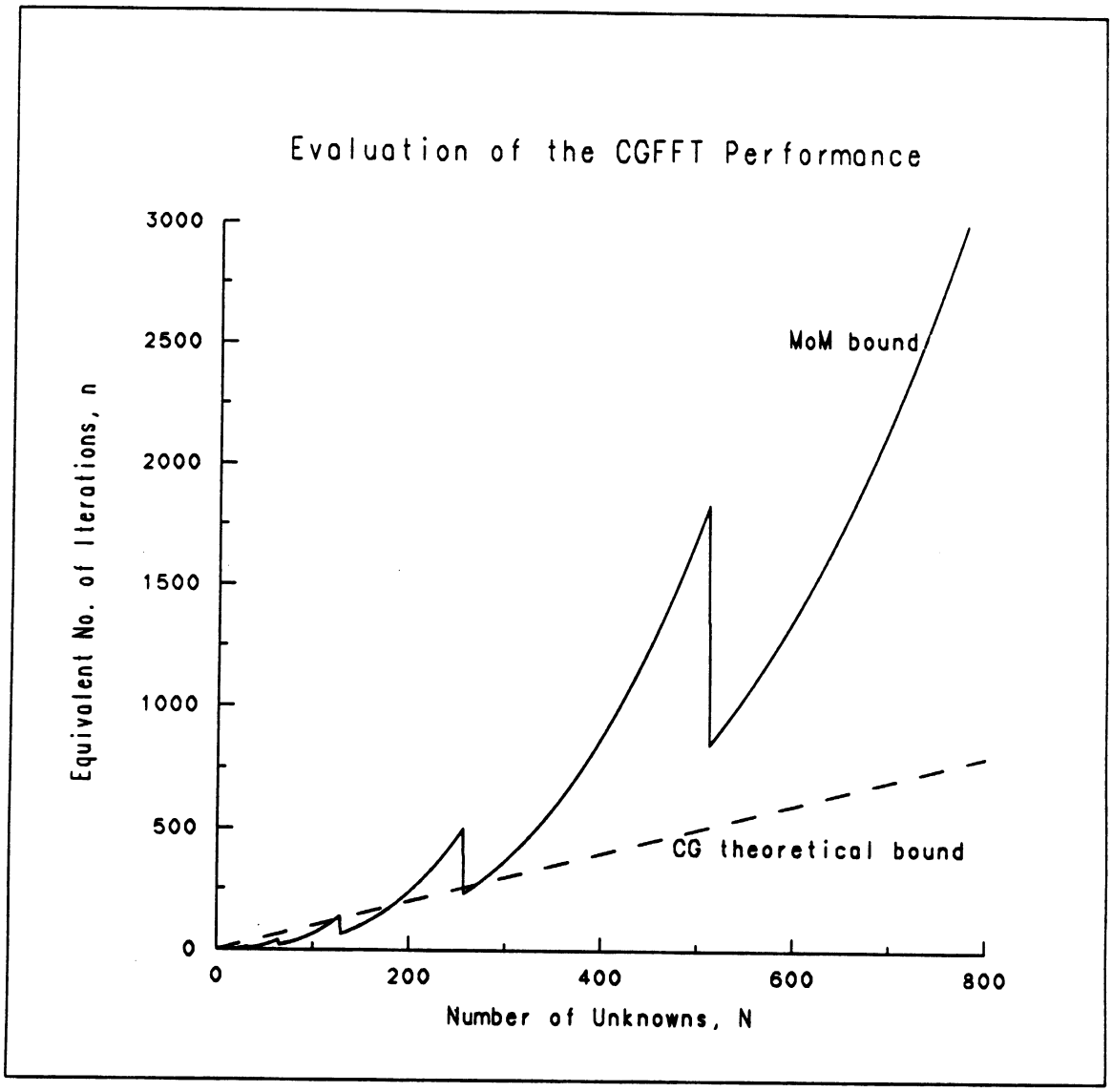

Figure 6.3: The bounds on the equivalent number of iterations for CGFFT based on table 6.1

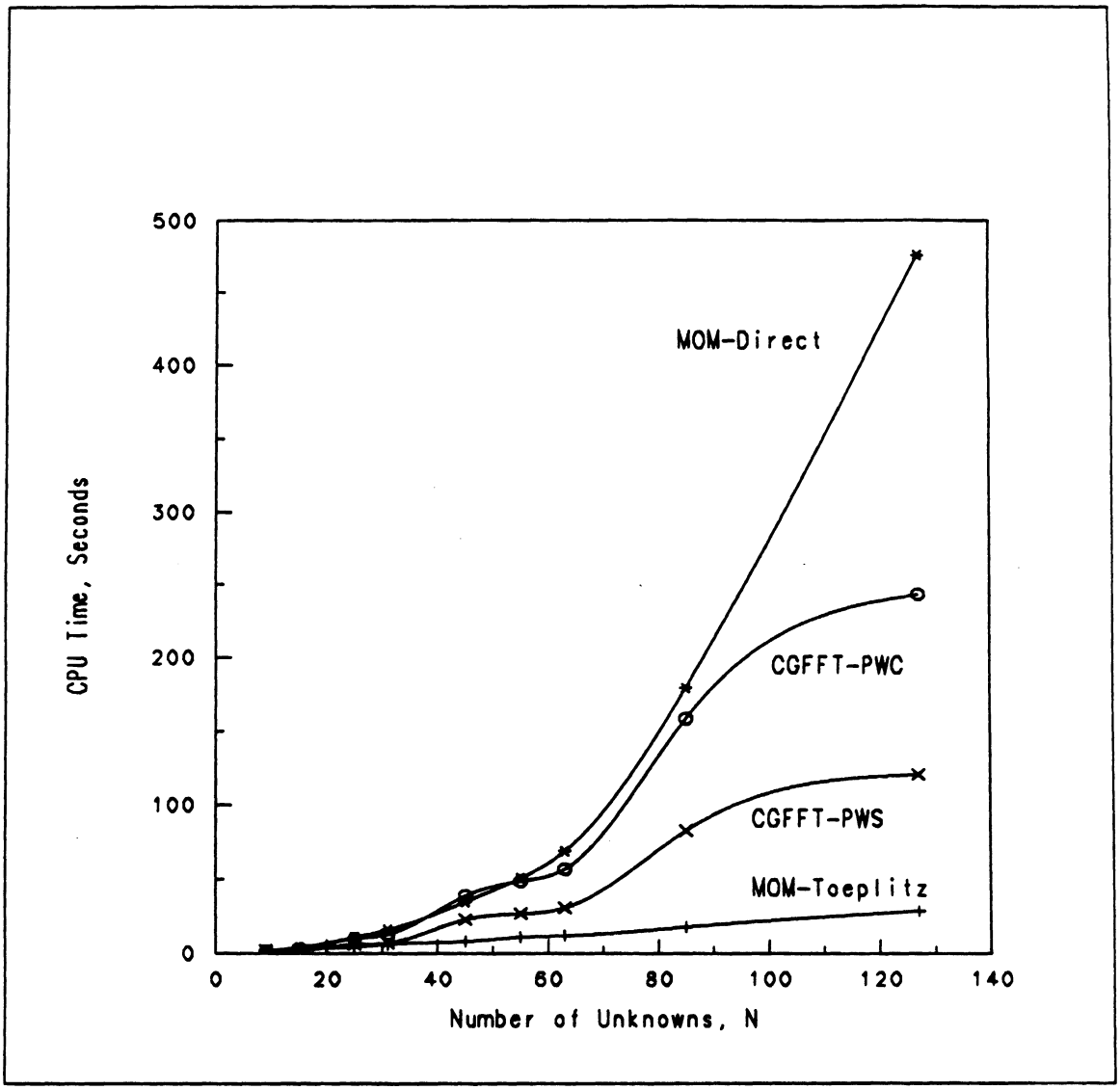

Figure 6.4: A comparison of the CPU time required by the MOM and the CGFFT formulations for the solution of the 1λ wire dipole problem.

Appendix A

Convergence of the Subsectional Basis Expansions

A.1 Vanishing End-Points

Let $u(x)$ be a continuous function with continuous first and second derivatives satisfying the Dirichlet boundary condition(Fig. A.1)

$$u(0) = u(l) = 0. \tag{A.1}$$

A piecewise approximation to $u(x)$ in terms of a sequence of basis functions $\{f_n\}$ is given by

$$u_N(x) = \sum_{n=1}^{N} u_n f_n(x) \quad , \quad h = l/N \tag{A.2}$$

where functions f_n have compact support over interval n with vanishing end-points and form a sequence of mutually orthogonal functions(except, perhaps for adjacent ones). Noting that $u_n = u(nh) = u_N(nh)$, it is of interest to show the convergence of this approximation to the given function $u(x)$ as the sampling interval decreases. To this end, the error introduced by the discretization of the function on any

subinterval $(n-1)h \leq x \leq nh$ is expressed as

$$v(x) = u(x) - u_N(x)\cdot \tag{A.3}$$

By expanding v and its first and second derivatives in Fourier sine series it can be shown that[18]

$$D_h^n(v) = \int_{(n-1)h}^{nh} (v'(x))^2 dx \leq \frac{h^2}{l^2} \int_{(n-1)h}^{nh} (v''(x))^2 dx \tag{A.4}$$

upon adding and noting that $|v''(x)| \leq |u''(x)|$ in the subintervals

$$D(u - u_N) \leq \frac{h^2}{l^2} \int_0^l (u''(x))^2 dx \cdot \tag{A.5}$$

Thus, the approximations converge in the Dirichlet energy norm at the rate h^2. An upper bound on the Hilbert norm of the residual can be obtained as well by employing the Poincare' inequality[18] which holds for any continuous function with continuous first derivative on an interval h and vanishing at the end-points. The inequality is

$$\int_0^h v^2(x) dx \leq h^2 D_n^h(v) \tag{A.6}$$

and when applied to (A.5), it gives

$$\int_0^l v^2(x) dx \leq h^2 D(u - u_N) = \frac{h^4}{l^2} \int_0^l (u''(x))^2 dx \tag{A.7}$$

which establishes the convergence of the approximation in the mean square sense as the sampling interval decreases.

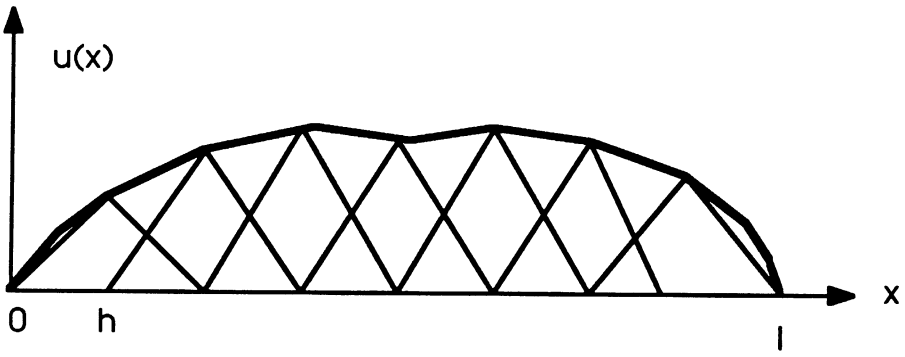

Figure A.1: A continuous function with vanishing end-points.

A.2 Singular End-Points

Assuming now that the function $u(x)$ is singular at the two end-points(Fig. A.2), the mean square residual may be expressed as

$$\begin{aligned}\int_0^l |u(x)-u_N(x)|^2dx &= \lim_{\epsilon\to 0}\int_\epsilon^h |u(x)-u_N(x)|^2dx + \int_h^{l-h} |u(x)-u_N(x)|^2dx \\ &+ \lim_{\epsilon\to 0}\int_{l-h}^{l-\epsilon} |u(x)-u_N(x)|^2dx. \end{aligned} \tag{A.8}$$

The second term on the right hand side is bounded because the above treatment may be applied by forming a Dirichlet problem for each interval and applying the Poincare' inequality to each segment. The inequality, however is no longer valid close to the singular region and one must resort to other methods to show convergence. A weaker bound can be established by rewriting the singular terms in the above equation and applying the triangle inequality. Considering the first term,

$$\begin{aligned}\lim_{\epsilon\to 0}\int_\epsilon^h |u(x)-u_1f_1(x)|^2dx &\le \int_0^h |u(x)|^2dx + \int_0^h |u_1f_1(x)|^2dx \\ &\le \int_0^h |u(x)|^2dx + h|u(h)f_1(h)|^2. \end{aligned} \tag{A.9}$$

Again, the second member on the right side of the above equation is finite and it remains to show that $\lim_{h\to 0}\int_0^h |u(x)|^2dx = 0$ which is true if the current grows to infinity slower than $1/\sqrt{x}$ as the edge is approached. This is in fact guaranteed by the edge condition which requires that the electromagnetic energy in a finite neighborhood of the edge to be finite[19].

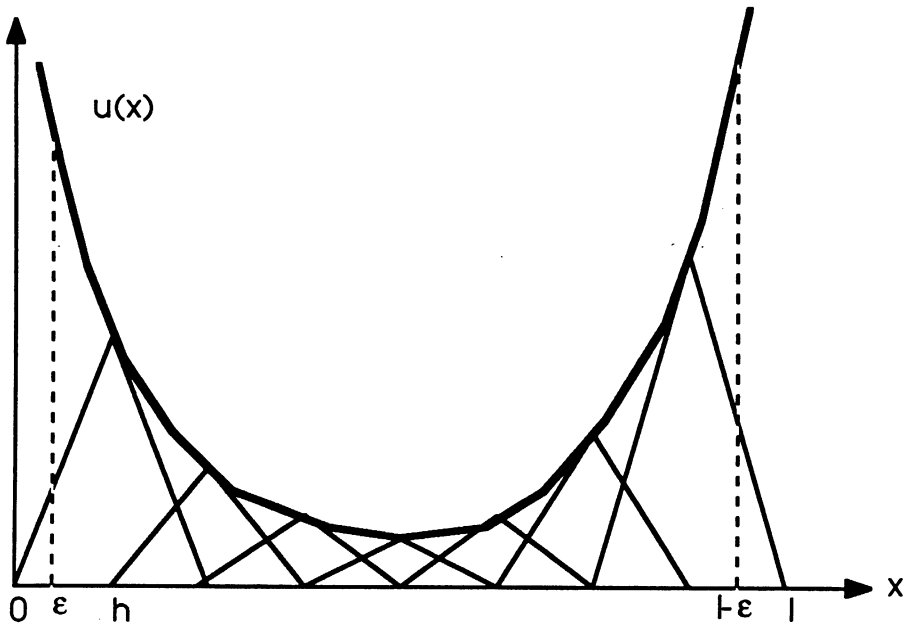

Figure A.2: A continuous function with singular end-points.

Appendix B

Numerical Considerations

The Fourier transforms in (3.9) and (4.18) are carried out discretely by a radix 2 FFT routine. The sampling interval is chosen small enough to satisfy Nyquist criterion and thus avoiding aliasing. However, due to the periodic representation of the function and its transform in the Discrete Fourier Transform (DFT), this operation results in the circular convolution rather than the desired linear convolution. The periodicity constraint results in an overlap of the convolution of one period to that of the succeeding period. To avoid these discrepancies, the period, N' of the array to be transformed is chosen so that[5]:

$$N' = 2^{\gamma} : N' > N_{Nyquist}, N' > 2 \times N - 1 \tag{B.1}$$

where N is the number of unknowns and γ is an integer. In practice γ is chosen according to the rule

$$\gamma \geq \log_2(2N - 1) + \rho \tag{B.2}$$

where ρ is an integer (usually unity) setting the *order* of the pad dimension to ensure adequate frequency sampling in the spectral domain when performing the

inverse transform operation. The discrete transform variable, k is defined as

$$k = k_0 \frac{l}{N'\Delta} \quad , -\frac{N'}{2} \leq l \leq \frac{N'}{2} - 1 \quad , \tag{B.3}$$

where Δ is the sampling interval and k_0 is the free space wave number. The array elements beyond the antenna's physical range are set to zero.

Appendix C

Dipole Input Impedance

C.1 Dipole Excitation Models

Two excitation models commonly used in the analysis of the wire antennas, namely the voltage gap model and the magnetic frill model are considered here.

C.1.1 Voltage Gap Model

In this model the source arises from the assumption that a finite voltage is placed across the antenna gap of width δ giving rise to an impressed electric field which is entirely confined to the gap. Thus, no fringing fields exist outside the gap region and the impressed field is expressed as

$$E^i = V/\delta \quad . \tag{C.1}$$

C.1.2 Magnetic Frill Model

The magnetic frill model is of practical significance specially in the modeling of a coaxial line feeding a monopole on a ground plane(Fig. C.1). Assuming that the coaxial structure supports a purely TEM aperture field of the form

$$E_\rho(\rho) = \frac{1}{2\rho \ln(b/a)} \quad ,$$

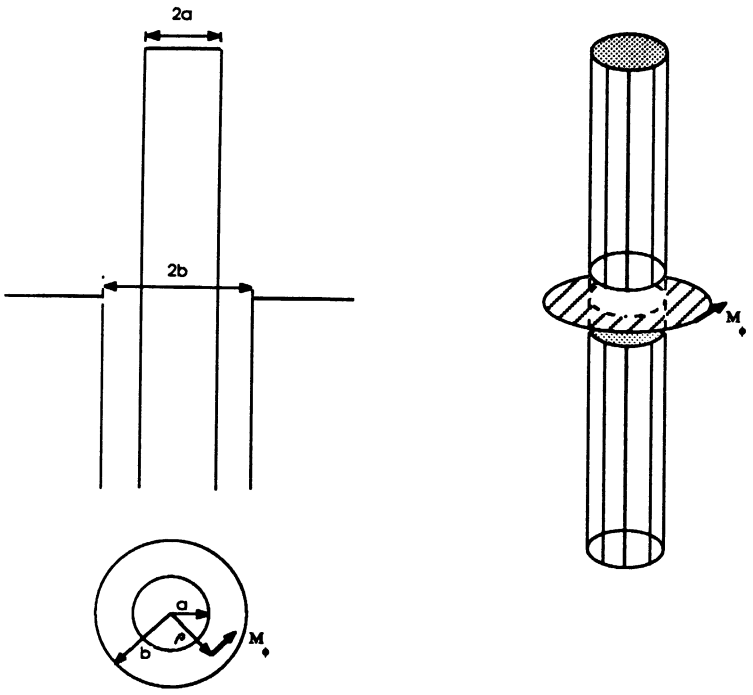

Figure C.1: The magnetic frill model.

the aperture and the ground plane are replaced with a frill of magnetic current using the image theory. The corresponding magnetic current distribution is

$$\begin{aligned} \mathbf{M} &= -\hat{n} \times \mathbf{E} \\ &= -\hat{\phi}\frac{1}{\rho \ln(b/a)} \end{aligned} \tag{C.2}$$

from which the electric field can be found by using the vector Hertz potential of magnetic type. The exact expression for the field on the axis of the antenna is[20]

$$E_z^i(0,z) = \frac{1}{2\ln(b/a)}\left(\frac{e^{-jkR_1}}{R_1} - \frac{e^{-jkR_2}}{R_2}\right)$$

where

$$R_1 = \sqrt{z^2 + a^2}$$

and

$$R_2 = \sqrt{z^2 + b^2}.$$

This expression gives a nonzero value for the incident field on every point along the wire antenna and accounts for the fringing fields outside the region of the generator.

C.2 Input Impedance

Once the current distribution on the cylindrical body is known, the input impedance can be computed based on power relations. From Poynting theorem,

$$\frac{1}{2}I(0)I^*(0)Z_{in} = \frac{1}{2}\int_s \mathbf{E}\times\mathbf{H}^*\cdot\mathbf{ds} \tag{C.3}$$

$$Z_{in} = -\frac{1}{|I(0)|^2}\int_{-l}^{l} E_z(a,z')I^*(z')dz', \tag{C.4}$$

where E_z is the tangential scattered electric field

$$E_z = E_z^s(a,z) = -E_z^i. \tag{C.5}$$

Thus, the input impedance is written in the form

$$Z_{in} = \frac{1}{|I(0)|^2}\int_{-l}^{l} E_z^i(a,z')I^*(z')dz'. \tag{C.6}$$

For a voltage gap model, the above equation reduces to the well known Ohm's law:

$$Z_{in} = \frac{V_0}{|I(0)|}. \tag{C.7}$$

Appendix D

Radiation Pattern of a Short Hertzian Dipole in the Presence of a Plate

D.1 Fields of a Hertzian Dipole Illuminating a Plate

The near field components of an infinitesimal Hertzian dipole ($l \leq \lambda/50$) oriented in the $\hat{z'}$ direction with its center positioned at a point $O'(x_1, y_1, z_1)$ can be expressed in the dipole coordinate system as(Fig. D.1)

$$E_{r'} = 2Z_0 I_0 k_0 l \frac{1}{k_0 r'}(1 + \frac{1}{jk_0 r'})\frac{e^{-jk_0 r'}}{4\pi r'}(\hat{z'} \cdot \hat{r'}) \tag{D.1}$$

$$E_{\theta'} = iZ_0 I_0 k_0 l(1 + \frac{1}{jk_0 r'} - \frac{1}{(k_0 r')^2})\frac{e^{-jk_0 r'}}{4\pi r'}\sqrt{1 - (\hat{z'} \cdot \hat{r'})^2} \tag{D.2}$$

$$E_{\phi'} = 0. \tag{D.3}$$

The associated unit vectors are expressed in unprimed coordinates so that

$$\hat{z'} = \sin(\theta_r)\cos(\phi_r)\hat{x} + \sin(\theta_r)\sin(\phi_r)\hat{y} + \cos(\theta_r)\hat{z}, \tag{D.4}$$

where θ_r and ϕ_r specify the orientation of the dipole relative to the plate. Also

$$\hat{r'} = \mathbf{r'}/|\mathbf{r'}| \tag{D.5}$$

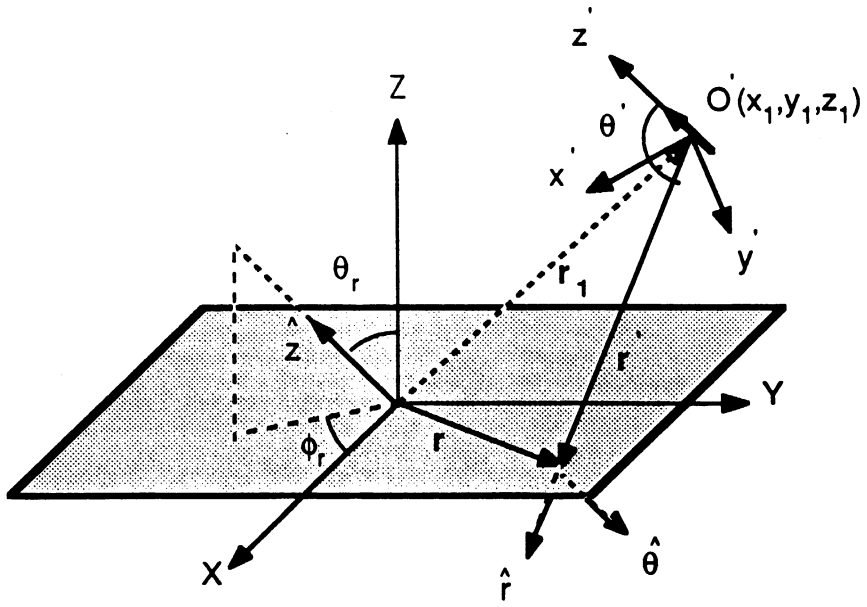

Figure D.1: An arbitrarily oriented Hertzian dipole above a plate with the associated coordinate systems.

with

$$\mathbf{r}' = \mathbf{r} - \mathbf{r}_1 \tag{D.6}$$

and

$$\hat{\theta}' = \frac{(\hat{z}' \times \hat{r}')}{|(\hat{z}' \times \hat{r}')|} \times \hat{r}'. \tag{D.7}$$

The field components can now be expressed in the unprimed coordinate system as:

$$E_x^i = (E_{r'}\hat{r}' + E_{\theta'}\hat{\theta}') \cdot \hat{x} \tag{D.8}$$

$$E_y^i = (E_{r'}\hat{r}' + E_{\theta'}\hat{\theta}') \cdot \hat{y} \tag{D.9}$$

$$E_z^i = (E_{r'}\hat{r}' + E_{\theta'}\hat{\theta}') \cdot \hat{z} \tag{D.10}$$

The incident fields are computed by using the above equations for observation points lying on the plate. These are then used in the operator equation as the known excitation.

D.2 Radiation Vector

The scattered field due to an induced polarization current on the plate can be expressed as

$$\mathbf{E}^s = -jk_0 Z_0 \frac{e^{-jk_0 r}}{4\pi r}\mathbf{N}_t \quad , \quad kr >> 1 \tag{D.11}$$

where $\mathbf{N}_t$ denotes the radiation vector

$$\mathbf{N}_t = \mathbf{N} - \hat{r}\mathbf{N}_r \tag{D.12}$$

with

$$\mathbf{N}(\theta,\phi) = \int_{s'} \mathbf{J}(\mathbf{r}')e^{jk\mathbf{r}'\cdot\hat{r}}ds' \quad . \tag{D.13}$$

Assuming a surface current density expansion of the form(Eq. 4.11)

$$\mathbf{J}(x,y) = f(x,y) * \sum_{n,m} \mathbf{J}_{nm}\delta(x - n\Delta x, y - m\Delta y), \tag{D.14}$$

the radiation vector can be computed numerically for the plate. It is given by

$$\mathbf{N}_t(\theta,\phi) = \tilde{f}(k'_x,k'_y)\sum_{n,m}\mathbf{J}_{nm}e^{-jk(n\Delta x k'_x + m\Delta y k'_y)} \tag{D.15}$$

where

$$\tilde{S}(k'_x,k'_y) = \int_x\int_y S(x,y)e^{-j(k'_x x + k'_y y)}dxdy$$

and

$$k'_x = k\sin\theta\cos\phi \quad , \quad k'_y = k\sin\theta\sin\phi\cdot \tag{D.16}$$

The total electric field is subsequently computed by adding the scattered field $\mathbf{E}^s$ and the dipole incident field given before in the far field.

Bibliography

[1] R. F. Harrington, *Field Computation by Moment Methods,* New York, Macmillan, 1968.

[2] M. R. Hestenes, *Conjugate Direction Methods In Optimization,* New York, Springer-Verlay, 1980.

[3] G. Strang, *Introduction to Applied Mathematics,* Massachusetts,Wellesley-Cambridge, 1980.

[4] J. W. Cooley and J. W. Tukey, "An algorithm for the machine calculation of complex Fourier series," *Mathematics of Computation,* vol. 19, No. 90, pp. 297-301, 1965.

[5] E. O. Brigham, *The Fast Fourier Transform,* Englewood Cliffs, New Jersey, Prentice-Hall, 1974.

[6] T. K. Sarkar, A. Ercument and M. Rao, "Application of FFT and the conjugate gradient method for the solution of electromagnetic radiation from electrically large and small conducting bodies," *IEEE Trans. Antenna Propagat.,* vol. AP-34, No. 5, pp. 635-640, May 1985.

[7] A. F. Peterson and R. Mittra, "Iterative-based computational methods for electromagnetic scattering from individual or periodic structures", *IEEE Trans. Antenna Propagat.,* vol. OE-12, No.2, pp. 458-465, Apr 1987.

[8] T. J. Peters and J. L. Volakis, "The application of a conjugate gradient FFT method to scattering from thin planar material plates," *IEEE Trans. Antenna Propagat.,*

[9] T. K. Sarkar, "Application of the conjugate gradient method for the solution of operator equations arising in electromagnetic scattering from wire antennas," *Radio Science,* vol. 19, No. 5, pp. 1156-1172, Sep-Oct 1984.

[10] N. N. Bojarski, "k-space formulation of the electromagnetic scattering problem," Tech. Rep. AFAL-TR-71-5,Mar 1971.

[11] W. L. Ko and R. Mittra, "A new approach based on a combination of integral equation and asymptotic techniques for solving electromagnetic scattering problems," *IEEE Trans. Antenna Propagat.,* vol. AP-25, No.2, pp. 187-198, Mar 1977.

[12] D. Borup and O. P. Gandhi "Faster Fourier transform method for calculation of SAR distribution in finely discretized inhomogeneous models of biological bodies," *IEEE Trans. Microwave Theory Tech.,* vol. MTT-32, Apr 1984.

[13] S. A. Bokhari and N. Balakrishnan, "A method to extend the Spectral-Iteration Technique," *IEEE Trans. Antenna Propagat.,* vol. AP-34, No.1, pp. 51-57, Jan 1986.

[14] R. F. Harington, *Time-Harmonic Electromagnetic Fields,* New Jersey, McGraw-Hill, 1961.

[15] I. S. Gradshteyn, I. M. Ryzhik, *Table of Integrals, Series, and Products,* New York, Academic Press, sec. 6.616-3, 1981.

[16] T. B. A. Senior and J. L. Volakis "Sheet simulation of a thin dielectric layer," *Radio Sci.,* Vol. 22, No. 7, pp. 1261-1272, Dec. 1987.

[17] E. Newman and D. M. Pozar, "Electromagnetic modelling of composite wire and surface geometries," *IEEE Trans. Antenna Propagat.,* vol. AP-26, pp. 784-789, Nov. 1978.

[18] K. E. Gustafson, *Introduction to Partial Differential Equations and Hilbert Space Methods* , New York, John Wiley & Sons, 1980.

[19] J. Meixner, "The behavior of electromagnetic fields at edges," *IEEE Trans. Antenna Propagat.,* vol. AP-20, No.4, pp. 442-446, Jul. 1972.

[20] L. L. Tsai, "A numerical solution for the near and far fields of an annular ring of magnetic current," *IEEE Trans. Antenna Propagat.,* vol. AP-20, pp. 569-576, 1972.